

1                   **Effects of uncertainties in the atmospheric density on the**  
2                   **probability of collision between space objects**

3                   **Charles D. Bussy-Virat<sup>1</sup>, Aaron J. Ridley<sup>1</sup>, Joel W. Getchius<sup>2</sup>**

4                   <sup>1</sup>Department of Climate and Space Sciences and Engineering, University of Michigan, Ann Arbor, Michigan, USA

5                                   <sup>2</sup>Omitron Inc., Beltsville, Maryland, USA

Author Manuscript

This is the author manuscript accepted for publication and has undergone full peer review but has not been through the copyediting, typesetting, pagination and proofreading process, which may lead to differences between this version and the [Version of Record](#). Please cite this article as doi: [10.1029/2017SW001705](https://doi.org/10.1029/2017SW001705)

Corresponding author: Charles Bussy-Virat, [cbv@umich.edu](mailto:cbv@umich.edu)

This article is protected by copyright. All rights reserved.

## Abstract

The rapid increase of the number of objects in orbit around the Earth poses a serious threat to operational spacecraft and astronauts. In order to effectively avoid collisions, mission operators need to assess the risk of collision between the satellite and any other object whose orbit is likely to approach its trajectory. Several algorithms predict the probability of collision but have limitations that impair the accuracy of the prediction. An important limitation is that uncertainties in the atmospheric density are usually not taken into account in the propagation of the covariance matrix from current epoch to closest approach time. The atmosphere between 100 km and 700 km is strongly driven by solar and magnetospheric activity. Therefore, uncertainties in the drivers directly relate to uncertainties in the neutral density, hence in the drag acceleration. This results in important considerations for the prediction of Low Earth Orbits, especially for the determination of the probability of collision. This study shows how uncertainties in the atmospheric density can cause significant differences in the probability of collision and presents an algorithm that takes these uncertainties into account to more accurately assess the risk of collision. As an example, the effects of a geomagnetic storm on the probability of collision are illustrated.

## 1 Introduction

The population of objects in orbit around the Earth has dramatically increased in the past decade. In April 2005, NASA performed its first collision avoidance maneuver on a robotic spacecraft (Terra satellite). Two years later, the Chinese satellite Fengyun-1C was destroyed, causing the largest increase in debris in space history (about 3,000 objects larger than 10 cm). On February 10th, 2009, the collision between the operational communication satellite Iridium 33 and the retired Russian communication satellite Cosmos 2251 generated 2,000 debris larger than 10 cm, with many thousands of smaller pieces at an altitude of 800 km. In 2015, four collision avoidance maneuvers and one “shelter-in-Soyuz” procedure were performed by the International Space Station (ISS) [Liou, 2016; Newman, 2016].

Collision avoidance requires the knowledge of the position and velocity of all objects in orbit. Some satellite mission operators can keep track of their satellites quite accurately using GPS data, but the trajectories of other orbiting objects are harder to accurately specify. Space Situational Awareness (SSA) refers to the effort of gathering and

38 updating the trajectories of natural and man-made orbiting objects [Stoll *et al.*, 2013]. Two  
39 of the organizations that support the SSA process are the Joint Space Operations Center  
40 (JSpOC), part of the 18th Space Control Squadron (18th SPCS), and the Space Data As-  
41 sociation (SDA). The SDA was established for satellite operators to share the most up-  
42 to-date satellite data [Stoll *et al.*, 2013]. JSpOC is currently the single full time global  
43 provider of object positions used in collision avoidance due to the accuracy and timeli-  
44 ness of the available information [Aida *et al.*, 2015]. It tracks more than 23,000 objects to  
45 evaluate the risk of collision with operating satellites by looking for any close approach  
46 with cataloged objects. If a potential conjunction is predicted by JSpOC, a Conjunction  
47 Data Message (CDM) is generated, which includes information about the close approach  
48 to alert the mission operator of a possible encounter. To evaluate the risk of collision, the  
49 probability of collision  $P_c$  is calculated based on the covariance matrices and the states of  
50 both objects at the Time of Close Approach (TCA). This step is part of the Conjunction  
51 Assessment Risk Analysis (CARA).

52 In order to perform CARA, the probability of collision must be accurately deter-  
53 mined. This is done by comparing the covariance matrices of the two objects at the time  
54 of closest approach. A covariance matrix represents the uncertainties in the state of the  
55 object. The  $i$ -th diagonal element corresponds to the variance of the  $i$ -th parameter (square  
56 of the standard deviation). The off-diagonal element  $i, j$  is proportional to the correlation  
57 coefficient between the  $i$ -th and the  $j$ -th elements. The position portion of the covariance  
58 matrices of each of the two objects can be represented by an ellipsoid, with an orientation  
59 given by the principal axes of the covariance matrix. Two such ellipsoids are illustrated in  
60 Figure 1.

61 **Figure 1.** Ellipsoids surrounding the primary and secondary spacecraft to represent the uncertainties in the  
62 positions of each object (Satellite Tool Kit (STK) - Analytical Graphics, Inc (AGI)).

63 The volume of intersection of the two ellipsoids is a representation of the probabili-  
64 ty of collision of the two objects. Computing this intersection volume implies calculating  
65 a three-dimensional integral, which can be computationally intense and complex. There-  
66 fore, the relative motion is assumed to be rectilinear so the derivation can be reduced to a  
67 two-dimensional integral in the plane normal to the relative velocity vector, called the con-

68 junction plane [Hejduk and Frigm, 2015; Sanchez-Ortiz et al., 2015]. Moreover, the orbit  
 69 uncertainties of the primary object are assumed to be uncorrelated with the orbit uncer-  
 70 tainties of the secondary object so the two covariance matrices can be combined in a sin-  
 71 gular covariance matrix [Chan, 2008]. Finally, the position uncertainties of the two objects  
 72 are assumed constant during the encounter so the combined covariance matrix is constant  
 73 during the close approach. These assumptions are valid if the duration of the encounter  
 74 is short enough ( $< 500$  s) or equivalently if the relative velocity between the primary and  
 75 secondary objects is high enough ( $> 10$  km/s) [Hejduk and Frigm, 2015]. The probabil-  
 76 ity of collision,  $P_c$ , is then expressed as [Sanchez-Ortiz et al., 2015; Akella and Alfriend,  
 77 2000; Alfriend et al., 1999; Foster, 2001]:

$$78 \quad P_c = \frac{1}{2\pi\sqrt{\det(C)}} \int_{-R}^R \int_{-\sqrt{R^2-x^2}}^{\sqrt{R^2-x^2}} e^{-\frac{1}{2}\vec{r}^T C^{-1}\vec{r}} dz dx \quad (1)$$

79 where  $R$  is the sum of the two object radii,  $\vec{r}$  the vector between the point of interest in  
 80 the conjunction plane and each point  $(x, z)$  is in the circle of radius  $R$  (integration area).  
 81 Most of the satellites don't have a spherical shape, in which case their radius can be de-  
 82 fined as their largest dimension.

83 Others have modified this technique. *Patera* [2001] used the symmetric form of the  
 84 probability density to reduce the 2D integral to a 1D contour integral. The contour corre-  
 85 sponds to the perimeter of the 2D integration area. This method provides an easier numer-  
 86 ical implementation and is computationally faster. *Patera* [2005] used numerical quadra-  
 87 ture techniques to transform the contour integral to a 1D angular integral by shifting the  
 88 origin of the coordinate system. *Alfano* [2005a] reduced the 2D integral into a 1D inte-  
 89 gral using the error function and analyzed it applying the Simpson's one-third rule. *Chan*  
 90 [2008] introduced the Rician function to approximate the 2D integral as a 1D integral over  
 91 a circle with an area equivalent to the elliptical cross-section area.

92 Although these methods are numerically easy to implement and computationally ef-  
 93 ficient, they rely on multiple assumptions that do not necessarily hold in every conjunction  
 94 case. *Alfano* [2009] assessed *Patera's* and *Alfano's* methods for linear relative motion and  
 95 showed important differences with the baseline Monte Carlo method, particularly when  
 96 the relative motion assumption does not hold, where errors up to 60% were found. Other  
 97 methods, that do not assume linear relative motion (*Adjoining Cylinders's* method [Alfano,  
 98 2005b], *Bundled Parallelepipeds's* method [Alfano, 2005b], and method of *Voxels* [Alfano,  
 99 2006]) also resulted in large errors because of limiting assumptions. Monte Carlo proce-

100 dures do not require the relative motion to be linear or the covariance matrices to be con-  
101 stant during the encounter. Therefore, the collision risk assessment can be more accurate  
102 in theory. The main drawback of the Monte Carlo approach is that it is computationally  
103 intensive. This method is presented in detail in Section 2.

104 *Alfriend et al.* [1999] investigated the sensitivity of the probability of collision to er-  
105 rors in the covariance matrix and to the encounter geometry. The study underlined the fact  
106 that although the position covariance at epoch is accurate, the velocity covariance is too  
107 optimistic because it assumes the dynamic model is perfect. Specifically, the uncertainties  
108 in the atmospheric density are usually not taken into account. As a result, when such un-  
109 certainties are not considered, the position uncertainties at the time of close approach are  
110 too optimistic by about an order of magnitude. *Alfriend et al.* [1999] showed that small  
111 errors in the covariance matrix can cause important changes in  $P_c$ .

112 At LEO altitudes, one of the main forces acting on spacecraft and debris is atmo-  
113 spheric drag and is a perturbing force particularly hard to model and predict. The drag  
114 acceleration  $\mathbf{a}_{\text{drag}}$  of a simple surface is represented by [Vallado and McClain, 2007]:

$$115 \quad \mathbf{a}_{\text{drag}} = -\frac{1}{2} \frac{C_D A}{m} \rho v_{\text{rel}}^2 \frac{\mathbf{v}_{\text{rel}}}{v_{\text{rel}}} \quad (2)$$

116 where  $C_D$ ,  $A$ , and  $m$  are the drag coefficient, area projected towards the velocity vector  
117 and mass of the surface respectively, and  $\mathbf{v}_{\text{rel}}$  is the satellite velocity with respect to the  
118 moving atmosphere of density  $\rho$ . The thermosphere is too dense to be neglected in ac-  
119 curate orbit calculations, particularly below  $\sim 500$  km. The atmosphere above about 100  
120 km is strongly coupled to the space environment. This system is very complex and the  
121 response of the density to driving from the ionosphere, magnetosphere, and Sun is very  
122 challenging to estimate. Moreover, the drivers of entire near-Earth space environment,  
123 mainly linked to solar activity, are themselves difficult to predict. Proxies are used to  
124 model these drivers, such as F10.7. This is the solar radio flux at a wavelength of 10.7 cm  
125 and it is commonly used to model Extreme UltraViolet (EUV) irradiance [Emmert, 2015].  
126 The perturbations of the Earth's magnetic field resulting from its interaction with the In-  
127 terplanetary magnetic Field (IMF) and the solar wind particles are described by magnetic  
128 activity indices such as Kp, Ap, Disturbance Storm Time (Dst), and Auroral Electrojet  
129 (AE). These indices can be derived from magnetic perturbations directly measured from  
130 stations on Earth.

131 Very few studies have analyzed the impact of uncertainties in the atmospheric drag,  
132 despite the fact that it is the largest source of errors for LEO orbits [Storz *et al.*, 2005;  
133 Emmert *et al.*, 2016]. By modeling the errors in EUV ten-day forecasts with a Brown-  
134 ian motion process, Emmert *et al.* [2014, 2016] derived an analytical equation that relates  
135 the uncertainties in F10.7 to uncertainties in the in-track position and found that the in-  
136 track position errors grow with time as  $\sim t^5$ . Although an analytical equation saves a lot  
137 of computational time, it does not provide a solution accurate enough for collision risk  
138 assessment. In particular, the solution assumes that the only perturbing force is atmo-  
139 spheric drag. However, neglecting the other perturbations can lead to important errors,  
140 in particular if neglecting the asphericity of the Earth. In addition, the effects of errors in  
141 the prediction of the solar proxies increase dramatically in the presence of a solar storm.  
142 D. Pachura [2016] showed that a miss prediction of a geomagnetic event leads to impor-  
143 tant changes in the probability of collision, up to a few orders of magnitude.

144 This study first presents an improvement of the Spacecraft Orbital Characterization  
145 Kit (SpOCK) to accurately predict the probability of collision between two space objects  
146 using Monte Carlo procedures. The algorithm models all perturbing forces and takes into  
147 account uncertainties in both F10.7 and Ap. The goal is to show how uncertainties in so-  
148 lar driver predictions result in important errors in the probability of collision. Addition-  
149 ally, the effects of a miss prediction of a geomagnetic storm on the probability of collision  
150 are demonstrated in an example. The algorithm developed can be used in real-time, and  
151 can provide mission operators with a better estimation of the risk of collision.

## 152 **2 Methodology**

153 The central capability of SpOCK is a high accuracy numerical propagator of space-  
154 craft orbits using a comprehensive model of the dynamics of spacecraft in orbit, including  
155 the asphericity of the Earth, atmospheric drag acceleration, solar radiation pressure and  
156 gravitational perturbations from the Moon and the Sun. Specifically, the non-spherical por-  
157 tion of the mass distribution of the Earth is modeled with a decomposition in spherical  
158 harmonics of the gravitational potential. Thermospheric models (Naval Research Labora-  
159 tory Mass Spectrometer Incoherent Scatter Radar Extended (NRLMSISE) [Picone *et al.*,  
160 2002] and the Global Ionosphere Thermosphere Model (GITM) [Ridley *et al.*, 2006]) are  
161 implemented in SpOCK to derive the atmospheric density at the position of the spacecraft  
162 and the time of interest, allowing for an accurate representation of the atmospheric drag.

163 In addition to modeling the motion of satellites, SpOCK includes several functionalities,  
164 such as the coverage of ground stations, the computation of solar power, and the storm  
165 intersection forecast tool developed for the CYclone Global Navigation Satellite System  
166 (CYGNSS) mission. Developed in C, SpOCK supports parallelism and is therefore well  
167 suited for ensemble, Monte Carlo, or satellite constellation analysis. The algorithm and its  
168 different functionalities are presented in *Bussy-Virat et al.* [2018].

## 169 **2.1 Conjunction Assessment Risk Analysis algorithm**

170 SpOCK can assess the risk of collision with other space objects in orbit (operational  
171 satellites or debris). Monte Carlo procedures are used to perturb the initial epoch state  
172 (position and velocity) of the primary and secondary spacecraft from the covariance matri-  
173 ces. The algorithm does not have to make any assumptions about the relative motion, the  
174 uncertainties in motion, or the covariances during the time span.

175 SpOCK is initialized with the state (position and velocity) and the covariance ma-  
176 trices of both space objects (noted  $\bar{O}_1$  and  $\bar{O}_2$ ) in the Earth Centered Inertial (ECI) J2000  
177 coordinate system ( $6 \times 6$  matrices). The sum of the two object radii,  $D_{\text{collision}}$ , and the  
178 threshold distance under which a close approach is flagged,  $D_{\text{CA}}$ , as well as the number of  
179 ensembles used in the Monte Carlo procedures, noted  $N_e$ , are also input.

180 The flow diagram in Figure 2 illustrates the process to evaluate the risk of collision  
181 that leads to the determination of the probability of collision between the two space ob-  
182 jects.

183 **Figure 2.** Flow diagram of SpOCK's CARA algorithm.

### 184 ***Close approach between the unperturbed orbits***

185 The first step in determining the probability of collision between two objects is to  
186 explore whether the orbits overlap. A first filter rules out the possibility of an encounter  
187 if the perigee of the higher object's orbit is greater than the apogee of the lower object's  
188 orbit. If this is not the case, the altitudes cross at some point, and the secondary object  
189 could present a potential threat. In that case, the two orbits are propagated to explore po-  
190 tential close approaches. The propagator uses a Fourth Order Runge-Kutta (RK4) method

191 with a fixed time step  $dt$  to integrate the acceleration and velocity at each time step  $t_i$  of  
 192 the simulation. A close approach is defined as any minimum in the distance between the  
 193 two objects smaller than a specified distance,  $D_{CA}$ . To determine if a minimum occurs  
 194 in each interval  $[t_i, t_{i+1}]$ , SpOCK uses a similar algorithm as Alfano-Negron Close Ap-  
 195 proach Software (ANCAS) [Alfano, 1994]. The flow diagram for this algorithm is pre-  
 196 sented in a separated block from the rest of the flow diagram in Figure 2 (black block at  
 197 bottom of the figure). First, it looks for the existence of a minimum in the distance be-  
 198 tween the objects by modeling the time derivative of the distance between the two objects  
 199 by a third-order polynomial,  $P_d$ , and assessing if any real root  $t_{root}$  exist in the interval  
 200  $[t_i, t_{i+1}]$ . The additional condition  $\frac{dP_d(t_{root})}{dt} > 0$  ensures the root corresponds to a min-  
 201 imum and not a maximum (not represented in Figure 2). If a root is found in the inter-  
 202 val  $[t_i, t_{i+1}]$ , the algorithm then determines the Distance of Close Approach (DCA) at  $t_{root}$   
 203 (now noted as TCA). The relative vector between the secondary and the primary objects  
 204 is noted  $\mathbf{r}_d = \mathbf{r}_2 - \mathbf{r}_1$ . SpOCK models the components  $r_{d,x}$ ,  $r_{d,y}$ , and  $r_{d,z}$  by fifth-order  
 205 polynomials  $P_{r_{d,x}}$ ,  $P_{r_{d,y}}$ , and  $P_{r_{d,z}}$ . The distance at close approach is then expressed as:

$$206 \quad DCA = \sqrt{P_{r_{d,x}}^2 + P_{r_{d,y}}^2 + P_{r_{d,z}}^2} \quad (3)$$

207 If  $DCA < D_{CA}$  then the situation is recorded as a close approach.

208 This operation is repeated for each interval  $[t_i, t_{i+1}]$  of the propagation.

### 209 *Initialization of perturbed orbits*

210 If a close approach between the two unperturbed orbits is found, there is a potential  
 211 risk for a collision. In that case, the Monte Carlo process is initialized at  $t_0$  (green dia-  
 212 gram second to top of Figure 2). The initialization consists in perturbing the ECI states of  
 213 the primary and secondary objects ( $\bar{U}_{1,t_0}$  and  $\bar{U}_{2,t_0}$ ). First, the covariance matrices (noted  
 214  $C_1$  for the primary object and  $C_2$  for the secondary object) are diagonalized and the two  
 215 sets of six eigenvalues derived. For each set of eigenvalue,  $N_e$  random vectors ( $6 \times 1$   
 216 for the position and the velocity) are generated following a Normal distribution centered  
 217 around 0 with a standard deviation equal to the square root of the eigenvalue of the co-  
 218 variance matrix:



$$\tilde{V}_{m,j} = \begin{pmatrix} \text{randn}(0, \sqrt{\lambda_{1,j}}) \\ \text{randn}(0, \sqrt{\lambda_{2,j}}) \\ \text{randn}(0, \sqrt{\lambda_{3,j}}) \\ \text{randn}(0, \sqrt{\lambda_{4,j}}) \\ \text{randn}(0, \sqrt{\lambda_{5,j}}) \\ \text{randn}(0, \sqrt{\lambda_{6,j}}) \end{pmatrix}$$

219 where  $\tilde{V}_{m,j}$  represents the  $m^{\text{th}}$  random vector ( $m = 1, \dots, N_e$ ) associated with the primary  
 220 ( $j = 1$ ) or secondary ( $j = 2$ ) object, and  $\lambda_{i,j}$  the  $i^{\text{th}}$  eigenvalue ( $i = 1, \dots, 6$ ) of the covari-  
 221 ance matrix  $C_j$ .

222 Each vector  $\tilde{V}_{m,j}$  is then converted back to the ECI coordinate system ( $\tilde{V}_{m,j,ECI}$ )  
 223 with the rotation matrix used for the diagonalization of the covariance matrix.

224 Finally, each perturbation  $\tilde{V}_{m,j,ECI}$  is added to the unperturbed ECI state to generate  
 225  $N_e$  perturbed states  $U_{m,1}$  and  $U_{n,2}$ :

$$U_{m,1,t_0} = \bar{U}_{1,t_0} + \tilde{V}_{m,1,ECI} \quad (4)$$

$$U_{n,2,t_0} = \bar{U}_{2,t_0} + \tilde{V}_{n,2,ECI} \quad (5)$$

226 Each ensemble member initialized as  $U_{m,j,t_0}$  is now noted  $O_{m,j}$ .

### 227 ***Conjunctions between the perturbed orbits***

228 Once the  $2N_e$  perturbed orbits are initialized, SpOCK propagates them (blue block  
 229 third to top in Figure 2). During the propagation, it screens for any conjunction between  
 230 a perturbed ensemble member  $O_{m,1}$  ( $m = 1, \dots, N_e$ ) of the primary object and a perturbed  
 231 ensemble member  $O_{n,2}$  ( $n = 1, \dots, N_e$ ) of the secondary object. The algorithm is the same  
 232 as the one to find a close approach between the unperturbed orbits  $\bar{O}_1$  and  $\bar{O}_2$ . However,  
 233 it now uses the sum of the two object radii  $D_{\text{collision}}$  as the minimum distance under which  
 234 a conjunction is recorded. Therefore, SpOCK first looks for the existence of a minimum  
 235 distance in each interval  $[t_i, t_{i+1}]$ , in which case it then calculates the minimum distance  
 236 as in Equation 3. If this distance is smaller than  $D_{\text{collision}}$ , the situation is recorded as a  
 237 collision. SpOCK repeats this operation for each combination in the set  $(m, n)$  resulting in  
 238  $N_e^2$  comparisons. The total number of collisions found is noted  $N_T$ .

239 To be computationally efficient, conjunctions between each perturbed orbit  $O_{m,1}$   
240 and  $O_{n,2}$  are not screened in every interval  $[t_i, t_{i+1}]$  of the propagation, but only in a time  
241 spanning the unperturbed close approach determined in the first step of CARA. This time  
242 span is equal to half an orbital period  $T$  to ensure that no collision is missed between the  
243 perturbed orbits. If several close approaches were found, then SpOCK applies this algo-  
244 rithm for each interval  $[TCA - T/4, TCA + T/4]$ .

### 245 *Derivation of the probability of collision*

246 Once the  $2N_e$  orbits are propagated and screened for collisions, the probability of  
247 collision is calculated as the ratio between the total number of collisions  $N_T$  divided by  
248 the total number of possible scenarios  $N_e^2$  (red block fourth to top in Figure 2):

$$249 P_c = \frac{N_T}{N_e^2} \quad (6)$$

250 This algorithm, presented in *Alfano* [2009], is commonly referred as the all-to-all  
251 strategy, as opposed to the one-to-one strategy that compares the position of each object  
252  $O_{m,1}$  to a single object  $O_{n,2}$ . It provides accurate estimates of the probability of collision  
253 in a reasonable computational time, although an accurate value of the confidence interval  
254 should be computed using other methods, such as the one-to-one strategy [*Schilling et al.*,  
255 2016]. If the one-to-one method was employed to compute the probability of collision  
256 though, it would involve the orbit propagation of more ensemble members, which would  
257 require a longer run-time (or the use of more cores) and would make this solution not eas-  
258 ily applicable for operations. Therefore, an empirical method for the determination of the  
259 confidence interval was used in this study to verify that the number of ensemble members  
260 considered was large enough to get an accurate estimation of  $P_c$  using the Monte Carlo  
261 approach. 50,000 ensemble members for each object were considered, which corresponded  
262 to a total number of possible scenarios  $N_e^2$  of 2.5 billions. To be computationally efficient,  
263 SpOCK runs the ensemble members in parallel, allowing the risk assessment of a two day  
264 scenario to be performed in an hour using 200 cores.

## 265 **2.2 Modeling uncertainties in F10.7 and Ap**

266 The uncertainty in the thermospheric density modeling is generally of the order of  
267 10-15% [*Vallado and Finkleman*, 2014] . This is when considering a perfect knowledge

268 of the inputs used in the thermosphere models, such as the solar flux F10.7, Ap, or Dst.  
269 However, predicting the solar drivers a few days ahead adds more uncertainties in the  
270 prediction of the thermospheric density. The large variability of the solar activity makes  
271 the task even harder. Geomagnetic activity driven by solar flares, Coronal Mass Ejection  
272 (CMEs), and Corotating Interaction Region (CIRs) cause the most important disturbances  
273 of the neutral density. For example, it was found that CIRs can cause density increases by  
274 75% on average [Lei et al., 2011]. A 30% to 60% increase at low to mid-latitudes in the  
275 density response to EUV solar flux enhancement resulting from a solar flare was reported  
276 in Sutton et al. [2006] and Pawlowski and Ridley [2011]. Bruinsma et al. [2006] and Sut-  
277 ton et al. [2005] studied the response to severe geomagnetic storms. Both noted a rapid  
278 response of the thermospheric density (~ a few hours) at all latitudes with enhancements  
279 by more than three times the density. Bruinsma and Forbes [2007] reported up to 800%  
280 density enhancements at the equator during sudden increases in geomagnetic activity.

281 Despite these considerations, collision risk assessment is usually performed by ne-  
282 glecting the uncertainties in the atmospheric density, although it recently became standard  
283 practice for the DoD to include atmospheric density errors in the covariance through the  
284 use of a consider parameter. At LEO altitudes, where atmospheric drag is the dominant  
285 perturbation, neglecting such uncertainties can result in important errors in the probability  
286 of collision.

287 SpOck primarily uses the NRLMSISE density model to derive the density at the  
288 position of the spacecraft at each time step of the propagation. The solar inputs of NRLM-  
289 SISE are the solar flux F10.7 and the geomagnetic index Ap. These are predicted in real  
290 time for the following 45 days at the Space Weather Prediction Center (SWPC) from the  
291 National Oceanic and Atmospheric Administration (NOAA). To model uncertainties in the  
292 predictions of F10.7 and Ap, historical predictions (noted  $P_{\text{predicted}}$ , where  $P$  is F10.7 or  
293 Ap) over two years were compared to actual measurements (noted  $P_{\text{measured}}$ ) as a function  
294 of prediction horizon. For each forecast time (1 day, 2 days, 3 days ahead), the difference  
295 between the predicted index and the measured value was computed ( $P_{\text{predicted}} - P_{\text{measured}}$ ),  
296 from which distributions were derived. Figure 3 shows the Probability Distribution Func-  
297 tion (PDF) of the F10.7 prediction error (top left) and the Ap prediction error (bottom  
298 left) for a 2-day forecast horizon. For every prediction horizon, each distribution is seg-  
299 mented in 7 bins from -15 and 15. For example, there is a 7% chance that the error on  
300 the prediction of F10.7 after 2 days is ~9 (red bin in top distribution) and there is a 35%

301 chance that the prediction of  $A_p$  is correct (green bin in bottom distribution). Although  
302 the distributions vary with the prediction horizon, since the accuracy of the forecast de-  
303 grades for longer prediction horizons, the PDFs are all centered around 0, indicating that  
304 the SWPC predictions were non-biased.

305 SpOCK uses these PDFs to model the uncertainties in the predictions of F10.7 and  
306  $A_p$ . Each graph on the right of Figure 3 shows an example of the 7 different 3-day pre-  
307 dictions of F10.7 (top) and  $A_p$  (bottom) on November 26th. A given prediction is derived  
308 as the sum of the value at the center of a bin in the PDF (reported in the legend) with the  
309 predicted value by SWPC. For instance, SWPC predicted F10.7 to be 83 and  $A_p$  to be 9  
310 on November 28. Therefore, the prediction of F10.7 corresponding to the red bin centered  
311 at 9 was 91. Similarly, the prediction of  $A_p$  corresponding to the light blue bin centered  
312 at -4 was 5. Applying this approach for each prediction horizon (1 day, 2 days, and 3 days  
313 ahead), SpOCK generated a series of predictions for F10.7 and  $A_p$ .

314 **Figure 3.** Probability Distribution Functions of the error in historical forecast of F10.7 (top left) and  $A_p$   
315 (bottom left). Prediction of the solar flux F10.7 (top right) and geomagnetic index  $A_p$  (bottom right) as a  
316 function of forecast time derived from these PDFs and the prediction by SWPC.

317 The Pearson correlation and the Kendall's tau coefficients of the historical forecast  
318 errors on F10.7 and  $A_p$  were respectively 0.02 and 0.009, indicating that they were un-  
319 correlated. Therefore, the F10.7 and  $A_p$  prediction errors were varied independently and  
320 input in NRLMSISE to model uncertainties in the prediction of the atmospheric density.  
321 Specifically,  $7 \times 7$  different combinations from the PDFs of the F10.7 and  $A_p$  prediction  
322 errors resulted in 49 density scenarios. The density modeled with NRLMSISE from these  
323 different solar activity conditions at a theoretical satellite location (at 400 km) is shown in  
324 Figure 4.

325 **Figure 4.** Atmospheric density at the position of the spacecraft as a function of forecast time modeled by  
326 NRLMSISE from the PDFs of the errors in historical F10.7 and  $A_p$  forecast (shown in Figure 3).

327 SpOCK uses real time predictions from SWPC and adds uncertainties to assess the  
328 risk of collision under different solar conditions. SpOCK propagates different ensembles,

329 consisting of thousands of members, through different thermospheres. Each individual  
330 ensemble is propagated through NRLMSISE driven by the same drivers, so the members  
331 can be realistically compared to each other. Different ensembles represent different density  
332 drivers, such that the dependence of the probability of collision on the density drivers can  
333 be explored. These simulations are run in parallel, which enables a quick evaluation of the  
334 range of possible values of the predicted probability of collisions, instead of one unique  
335 value as it is currently done in a typical conjunction risk assessment analysis.

### 336 **2.3 Modeling other uncertainties**

337 When assessing the true risk of collision, all uncertainties must be taken into ac-  
338 count. Uncertainties in the initial position and velocity are important because of the lim-  
339 ited availability and accuracy of tracking the object. The thermospheric density is the  
340 main source of uncertainties in the propagation of the spacecraft but, as shown in Equa-  
341 tion 2, it is not the only parameter of the drag acceleration. Uncertainties in the drag co-  
342 efficient and the cross section area are also important. The drag coefficient and the cross  
343 section area depend on the attitude of the satellite so they are sometimes combined into  
344 one single parameter, such as the ballistic coefficient ( $B_C = \frac{C_D A}{m}$ ). However, uncertainties  
345 in both parameters can be modeled separately in SpOCK. For most secondary objects with  
346 unknown drag coefficients and cross-section areas, the Monte Carlo procedures should  
347 include directly perturbing the ballistic coefficient from its variance estimated in the co-  
348 variance matrix.

349 The coefficient of drag  $C_D$  represents the transfer in momentum between the molecules  
350 of the atmosphere and the surfaces of the satellite. It is a function of the satellite shape  
351 and attitude, of the atmospheric conditions (temperature and composition), and of the  
352 properties of the satellites surfaces. It usually decreases with the altitude [*Moe and Moe,*  
353 *2005; Horsley, 2012*]. In order to model uncertainties in the drag coefficient, SpOCK  
354 initializes the properties of each surface of the ensemble members with drag coefficients  
355 computed from the covariance matrix at the initial epoch.

356 Modeling the uncertainty in the attitude for a controlled satellite that has a known  
357 attitude control uncertainty consists in having ensemble members that drift with a random  
358 angular velocity from a nominal attitude for a given time before going back to the nominal  
359 attitude. This enables the simulation of the attitude determination and control system of

360 satellites that randomly drift from a nominal controlled attitude. Additionally, objects that  
361 are uncontrolled can be simulated by setting nominal tumbling rates around the three axes,  
362 with uncertainties around those nominal rates also specified.

363 Although these different uncertainties need to be taken into account in a realistic  
364 collision risk assessment, this study focuses on exclusively modeling uncertainties in the  
365 initial positions and velocities, as well as in the thermospheric density.

### 366 **3 Validation**

367 To validate the conjunction assessment risk analysis algorithm in SpOOCK, the cu-  
368 mulative probabilities of collision computed for three different cases were compared with  
369 results from *Alfano* [2009]. More specifically, two LEO configurations (cases 6 and 7 in  
370 *Alfano* [2009]) and one GEO configuration (case 1 in *Alfano* [2009]) were analyzed. The  
371 initial states and covariance matrices, included in *Alfano* [2009], were used to initialize  
372 CARA in SpOOCK. *Alfano* [2009] used a similar CARA algorithm as SpOOCK's. In all  
373 three cases, the time of close approach is 2 days after the epoch. The dynamic model used  
374 a spherical Earth with no perturbations, since the goal of this study was to validate the al-  
375 gorithm for computation of the probability of collision, while SpOOCK's propagator and its  
376 dynamic model were validated in a previous study [*Bussy-Virat et al.*, 2018].

377 Figure 5 shows the cumulative distribution functions computed by SpOOCK for cases  
378 1 (top), 6 (center), and 7 (bottom). Similar figures are available in *Alfano* [2009] but  
379 are not shown here because they correspond to probabilities determined with a different  
380 method than the Monte Carlo approach. Therefore, a direct comparison of the cumulative  
381 probability as a function of time is not possible. However, the trends of the figures in *Al-*  
382 *fano* [2009] are very similar to the ones presented in Figure 5. Case 1 represent a nonlin-  
383 ear relative motion that causes the probability to increase again a few hours after the first  
384 close approach. Cases 6 and 7 correspond to a linear relative motion where the probabili-  
385 ty of collision starts growing a few minutes before the unperturbed close approach, with  
386 a faster increase for case 6. The text in each plot summarizes the results for the cumu-  
387 lative probability of collision calculated by SpOOCK and compared to the value in *Alfano*  
388 [2009]. The relative difference is smaller than 3% for the three cases, proving that both  
389 algorithms are in a good agreement. The small differences might be due to the fact that

390 *Alfano* [2009] used an analytic equation to propagate the covariance matrices from current  
391 epoch to time of closest approach.

392 **Figure 5.** Cumulative probability of collision during the half orbit spanning the unperturbed close approach.  
393 The vertical red dashed line represents the time of close approach between the two unperturbed orbits. The  
394 initial states and covariance matrices are taken from *Alfano* [2009]: top is case 1, center is case 6, and bottom  
395 is case 7.

## 396 **4 Results and discussion**

### 397 **4.1 Effects of atmospheric drag on the probability of collision**

398 To understand the effects of atmospheric drag on the probability of collision, a hy-  
399 pothetical collision between two satellites with slightly different velocities is considered.  
400 Both spacecraft start at their respective initial position and Satellite 2 is assumed to have  
401 the higher speed of the two satellites. The distance between the initial positions and the  
402 conjunction point are respectively noted  $D1$  and  $D2$ .

403 If the density of the atmosphere was actually higher than predicted, the increase in  
404 atmospheric drag would have more effect on Satellite 2 than on Satellite 1 because Satel-  
405 lite 2 is moving faster. In other words, Satellite 2's altitude would decrease faster than  
406 Satellite 1's, so Satellite 2's speed would increase more than Satellite 1's speed. There-  
407 fore, Satellite 2 would reach the distance  $D2$  before Satellite 1 reached the distance  $D1$ .  
408 Because of this differential change in speed, Satellite 2 would get to the conjunction point  
409 before Satellite 1 so the two satellites would potentially not collide anymore. Similarly,  
410 two spacecraft that were not predicted to collide could actually collide if the density was  
411 different from the prediction.

412 In the Monte Carlo method, a large number of such situations are considered. The  
413 total number of collisions in the Monte Carlo procedure therefore directly depends on the  
414 density of the atmosphere in which the spacecraft orbit. In other words, uncertainties in  
415 the predictions of the thermospheric density have an effect on the probability of collision.

## 4.2 Effects of uncertainties in the thermospheric density predictions on the probability of collision

SpOCK was run to assess the risk of collision between two hypothetical objects using the algorithm presented in Section 2. Both spacecraft orbited at 400 km with a 30° and 60° inclination respectively. The ECI states and covariance matrices at the initial epoch (12 am UTC on November 26th, 2016) are included in the appendix. A first collision risk assessment was performed using the median values of the F10.7 and Ap predictions of Figure 3 (bin centered at 0 in green), so the density was modeled using the predictions of F10.7 and Ap by SWPC. 50,000 ensemble members were propagated for each of the two satellites so the total number of possible encounters was 2.5 billion. The orbits were propagated with a 10 second time step and the gravitational perturbation due to the equatorial bulge ( $J_2$ ) was taken into account. The green line represents the orbit of Satellite 1 (30° inclination) and the magenta line represents the orbit of Satellite 2 (60° inclination). The closest approach was predicted to occur over the Pacific Ocean.

**Figure 6.** Top: 2D visualization of the two orbits. Satellite 1 (green line) orbits at 400 km with a 30° inclination and a 0° RAAN. Satellite 2 (magenta line) orbits at 400 km with a 60° inclination and a 30° RAAN. The right figure is a zoom in over a  $\sim 120 \text{ km} \times 120 \text{ km}$  region. Bottom: distance between the two unperturbed orbits over the first two days of the propagation. The close approach occurs on November 27th at 12 pm. The threshold distance for close approaches,  $D_{CA}$ , is indicated as a dashed horizontal line.

The relative distance over the first two days between the two unperturbed orbits is presented in the bottom plot of Figure 6. The time of closest approach was predicted to occur  $\sim 36$  hours after epoch, at noon on November 27th.

A zoom in of the encounter geometry is illustrated in Figure 6 (top right). Three 10 s time steps are represented around the time of closest approach. Object 1 is represented by green squares (smaller inclination) and Object 2 by magenta circles (higher inclination). The time of closest approach was predicted to be at 12:00:00.104, at  $\sim 21.75^\circ\text{N}$  latitude.

The minimum distance under which a close approach between the two unperturbed orbits was flagged was 10 km. Because this occurred, SpOCK's Monte Carlo algorithm presented in Section 2.1 assessed the risk of collision for this possible conjunction. The



446 sum of the two spacecraft radii was 1.3 m, implying that any situation with a distance be-  
447 tween an object  $O_{m,1}$  and an object  $O_{n,2}$  smaller than 1.3 m was recorded as a collision.

448 When this was completed, the probability of collision was  $1.051 \times 10^{-4}$ , right above  
449 the threshold for a collision avoidance maneuver ( $10^{-4}$ ) used by NASA (this threshold  
450 varies by individual NASA mission, though). The distribution of the time of closest ap-  
451 proach for each collision between a perturbed object  $O_{m,1}$  and a perturbed object  $O_{n,2}$  is  
452 shown in Figure 7. The 50% width of the distribution (defined as the difference between  
453 the 75% and the 25% quantiles) is  $\sim 300$  ms, which represents the uncertainty in the time  
454 of closest approach. This uncertainty is particularly small because of the encounter ge-  
455 ometry. For example, if the inclinations of the two orbits were similar, the velocities at  
456 conjunction would be almost parallel to each other. Since uncertainties are usually greater  
457 in the along-track direction, the range of values for the time of close approaches increases  
458 for such parallel conjunctions.

459 **Figure 7.** Distribution of the time of close approach for all conjunctions. The 25% and 75% quantiles are  
460 shown as vertical dashed lines.

461 To demonstrate the effects of uncertainties in the thermospheric density on the prob-  
462 ability of collision, the risk of collision was assessed with the different densities shown in  
463 Figure 4. More specifically, 49 cases were evaluated for collision risk assessment. Each  
464 case corresponded to the probability of collision between the two objects orbiting in an  
465 atmosphere whose density was represented by one of the 49 scenarios of Figure 4.

467 The time and distance of closest approach between the two unperturbed orbits, i.e.,  
468 using the nominal orbital parameters, for nine cases are represented in Table 1. These  
469 cases correspond to example trajectories that were generated by moving the F10.7 and  
470 Ap prediction errors in lock-step through the whole range of errors in order to span the  
471 entire spectrum of possibilities. The unperturbed orbits were not predicted to collide be-  
472 cause the distances at closest approach were greater than 1.3 m, but they were flagged to  
473 be investigated due to the distances being less than 10 km.

474 The higher the density, the more drag there is on the spacecraft, which leads to  
475 a lower orbital altitude and thus a higher orbital speed, resulting in earlier closest ap-

**Table 1.** Time and distance of close approach for different atmospheric density scenarios.

Case #	TCA	DCA (m)
1	2016-11-27 12:00:00.311	125
2	2016-11-27 12:00:00.213	106
3	2016-11-27 12:00:00.182	91.2
4	2016-11-27 12:00:00.124	64.3
5	2016-11-27 12:00:00.104	58.0
6	2016-11-27 12:00:00.075	42.6
7	2016-11-27 12:00:00.047	26.7
8	2016-11-27 11:59:59.989	1.61
9	2016-11-27 11:59:59.914	38.2

476 proaches. This can be noticed in Table 1 where the time of close approach gradually de-  
 477 creased from Case 1 (lowest densities) to Case 9 (highest densities) by  $\sim 400$  ms.

478 Figure 8 shows the positions of the two spacecraft on November 27th at 12:00:00 for  
 479 the nominal orbit condition for these nine different thermospheric conditions. This corre-  
 480 sponds to the time step preceding the close approach for all cases, except for Cases 8 and  
 481 9, for which it corresponds to the time step following the encounter. The increasing de-  
 482 lay between this snapshot and the encounter from Case 1 to Case 7 is evident in Figure 8.  
 483 Because the closest approach for Cases 8 and 9 occurred before the time of this snapshot,  
 484 the red and purple markers are located beyond the conjunction point (not represented in  
 485 the Figure for clarity).

486 **Figure 8.** Snapshot of the unperturbed orbits  $\bar{O}_1$  (square) and  $\bar{O}_2$  (circle) at 12:00:00 pm on November 27th,  
 487 2016. The two objects are about to collide for Cases 1, 2, 3, 4, 5, 6, and 7 and have just collided for Cases 8  
 488 and 9.

489 Added to the uncertainty of the time of closest approach between ensembles of the  
 490 same scenario (e.g., 300 ms, Figure 7), the total uncertainty on the time of close approach,  
 491 including uncertainties in the thermospheric densities, was  $\sim 700$  ms. This is a small un-  
 492 certainty and it does not cause any concern for operations because maneuvers are planned  
 493 hours in advance. However, this short uncertainty was due to the encounter geometry,

494 where the 2 objects approach with non parallel velocities. For parallel conjunctions, this  
495 uncertainty would grow dramatically.

498 Although the effects of density uncertainties on the time of closest approach were  
499 small for this geometrical configuration, the effects on the probability of collision were  
500 much more important. The likelihood of each of the 49 density scenarios to occur at  
501 TCA is given as the product of the likelihood of the prediction error in F10.7 to occur  
502 at TCA with the likelihood of the prediction error in Ap to occur at TCA, since the dis-  
503 tributions of the historical prediction errors of F10.7 and Ap are uncorrelated. Since the  
504 temporal resolution of the F10.7 and Ap predictions was 1 day, the likelihoods of the pre-  
505 diction errors in F10.7 and Ap were evaluated at +48h, instead of +36h (TCA). For in-  
506 stance, the likelihood of the error in F10.7 and Ap to be 9 and -4 respectively (red and  
507 light blue bins of the PDFs in Figure 3, respectively) was  $0.07 \times 0.16 \approx 0.011$ . In other  
508 words, the likelihood of occurrence of the density scenario modeled by NRLMSISE from  
509 the F10.7 and Ap values depicted in red and light blue in the right two graphs of Figure  
510 3 was  $\sim 1.1\%$ . Each of the 49 density scenarios in Figure 4 occurred with a probab-  
511 ility computed with the same method, resulting in 49 values of the probability of collision,  
512 which likelihood to occur was equal to the likelihood of occurrence of the corresponding  
513 density scenario. Figure 10 (left) shows the PDF of the probability of collision derived  
514 from the 49 values of  $P_c$  and their likelihood of occurrence. The probability of each  $P_c$   
515 interval to occur is equal to  $\sum_i P_{c,i} \times p_i$  (for all  $P_{c,i}$  in the interval), where  $p_i$  is the like-  
516 lihood of the probability  $P_{c,i}$  to occur. The peak of the PDF was obtained for  $P_c$  between  
517  $1.0 \times 10^{-4}$  and  $1.1 \times 10^{-4}$ , for which the probability of occurrence was larger than 30%.  
518 The cases with a probability of collision falling in this interval corresponded to densities  
519 modeled from values of F10.7 and Ap close to the SWPC predictions since these were the  
520 most likely to occur, as shown in the distributions of Figure 3. The PDF extended to val-  
521 ues of  $P_c$  as low as  $\sim 10^{-5}$ , although probabilities of occurrence of such scenarios were  
522 much lower ( $<5\%$ ). Overall, the expected probability of collision, equal to the sum of  
523 each  $P_c$  to occur multiplied by its likelihood of occurrence, was  $8.7 \times 10^{-5}$ , right below  
524 the maneuver threshold used by NASA. Figure 10 (right) shows the Cumulative Distribu-  
525 tion Function (CDF) of the probability of collision. The CDF gives the probability of  $P_c$   
526 to be below a certain threshold. For instance, the probability for  $P_c$  to be below  $8 \times 10^{-5}$   
527 or  $10^{-4}$  was  $\sim 25\%$  or  $\sim 85\%$ , respectively. While PDFs indicate the values of  $P_c$  that are

528 the most likely to occur, CDFs can help identify how much of the probability density is  
529 above or below a certain threshold.

496 **Figure 9.** Probability Distribution Function and Cumulative Distribution Function of  $P_c$  as a result of  
497 uncertainties in the atmospheric density. The PDF and CDF were segmented into bins of  $P_c$  of  $10^{-5}$ .

530 This analysis shows that uncertainties in the prediction of the thermospheric density  
531 can lead to important errors on the probability of collision if only the nominal predic-  
532 tion is considered for the collision risk assessment, even if the conjunction occurs only 36  
533 hours after the current epoch. More importantly, it provides an example of application of  
534 a framework that can assist collision avoidance practitioners to estimate the risk of colli-  
535 sion by providing a true probabilistic result for different  $P_c$  outcomes.

### 536 *Confidence interval*

537 An empirical method was used to compute the confidence interval associated with  
538 the estimations of the probability of collision. The scenarios that gave the minimum and  
539 maximum values of  $P_c$  ( $\sim 3 \times 10^{-5}$  and  $\sim 1 \times 10^{-4}$ , respectively) were considered to bound  
540 the solution. For each of these two scenarios, SpOCK was run 100 times and the confi-  
541 dence interval was computed from the distribution of the 100  $P_c$  values. Figure 10 shows  
542 the distributions corresponding to the 100 runs for the minimum value of  $P_c$  ( $\sim 3 \times 10^{-5}$ ,  
543 left) and for the maximum value of  $P_c$  ( $\sim 1 \times 10^{-4}$ , right). For each distribution, the me-  
544 dian value of  $P_c$  was computed,  $P_{c,\text{median}}$ , and the relative error on  $P_c$ ,  $\epsilon$ , was derived  
545 to include  $\sim 95\%$  of the  $P_c$  values in the interval  $[P_{c,\text{median}} \times (1 - \epsilon), P_{c,\text{median}} \times (1 + \epsilon)]$ .  
546  $\sim 95\%$  of the runs resulted in probabilities of collision different by less than 2.6% com-  
547 pared to the median value of the lowest probability of collision ( $\sim 3 \times 10^{-5}$ ), and by less  
548 than 1.6% compared to the median value of the highest probability of collision ( $\sim 1 \times 10^{-4}$ ).  
549 The larger distribution for the low value of  $P_c$  is consistent with the fact that more en-  
550 semble members should be run in order to get the same relative error as for the scenario  
551 with the larger value of  $P_c$ . The 47 other scenarios resulted in probabilities of collision  
552 between these two  $P_c$  extrema, so the relative error corresponding to a confidence interval  
553 of 95% for these scenarios was between 1.6% and 2.6%. Overall, although this empiri-  
554 cal method is an approximation, it provides an estimation of the confidence interval and

555 shows that the Monte Carlo approach used to compute the probability of collision for the  
556 previous example scenarios was relevant.

557 **Figure 10.** Distribution of the 100 estimated values of  $P_c$  (left:  $\sim 3 \times 10^{-5}$ ; right:  $\sim 1 \times 10^{-4}$ ). The confidence  
558 interval and relative error are indicated. The red dashed lines correspond to the boundaries of the interval  
559 that included  $\sim 95\%$  of the predicted values of  $P_c$ . The black dashed lines represent the median values of the  
560 distributions.

### 561 **4.3 Probability of collision errors due to a miss prediction of a solar storm**

562 In the previous section, the probability of collision was assessed given uncertain-  
563 ties in the thermospheric density during quiet conditions. In this section, the impact of  
564 a geomagnetic storm on the probability of collision is investigated. For this analysis, the  
565 geomagnetic storm occurring on March 17th, 2015 was studied. Two orbits were propa-  
566 gated for two days, starting on March 16th. The encounter geometry corresponded to a  
567 parallel path conjunction: both orbits were at an inclination of  $45^\circ$  at 400 km. Object 2's  
568 eccentricity is slightly higher than Object 1's eccentricity (0.00002 and 0.00001 respec-  
569 tively). This is a particularly interesting configuration as the assumption of short time of  
570 encounter used in many collision risk assessment algorithms does not hold for this parallel  
571 conjunction geometry.

572 The geomagnetic index  $A_p$  was reported to reach values as high as 200 on March  
573 17. The orbit averaged density modeled at the position of object 1 using NRLMSISE is  
574 shown in Figure 11. The red line shows the density modeled from the actual F10.7 and  
575  $A_p$ , while the blue line represents the density modeled with keeping F10.7 and  $A_p$  con-  
576 stant to the initial value on March 16th.

577 To study the effect of the storm on the probability of collision, two conjunction  
578 analysis simulations were made. The first one used the actual solar activity conditions to  
579 model the atmospheric density (red line in Figure 11). The second one used a constant  
580 solar activity for the two days of the simulations (blue line in Figure 11). This simulation  
581 corresponded to a situation without a geomagnetic storm, as if the predictions were for  
582 calm geomagnetic conditions instead of for a storm. For both runs, the risk of collision  
583 was assessed by SpOCK to compare the probability of collision and the time of conjunc-  
584 tion.

585 **Figure 11.** Orbit average density at the position of the spacecraft with the geomagnetic storm (red) and  
586 without the geomagnetic storm (blue).

587 Figure 12 shows the cumulative probability distribution function as a function of  
588 time for both simulations, defined as the total number of recorded collisions as a func-  
589 tion of time, divided by the total number of possible conjunctions. Consequently, the total  
590 cumulative probability of collision at the end of the span is equal to the probability of col-  
591 lision  $N_T/N$  used so far in the study. The red line corresponds to the simulation with the  
592 geomagnetic storm, and the blue line without it. The vertical dashed lines represent the  
593 times of closest approach between the unperturbed orbits, which are also indicated in the  
594 top left corner of the plot.

595 The conjunction occurred sooner in the presence of the storm by  $\sim 2$  seconds. This  
596 was due to a stronger drag because of the increase in density resulting from the effects of  
597 the geomagnetic storm on the thermosphere. Therefore, the satellites orbited with higher  
598 velocities and the close approach occurred sooner than without the storm.

599 The probability of collision in the absence of the storm was slightly above the ma-  
600 neuver threshold ( $1.13 \times 10^{-4}$ ), however, with the storm, the probability of collision was  
601  $8.80 \times 10^{-5}$ , which was under the maneuver threshold. This  $\sim 30\%$  difference in the prob-  
602 ability of collision not only demonstrates the important effect of the storm on the proba-  
603 bility of collision, but it also shows that if on March 16th, the space weather models had  
604 not predicted the storm to occur a day later, the predicted probability of collision would  
605 have been right above the maneuver threshold so the mission operator may have been ad-  
606 vised to perform a collision avoidance maneuver. This miss prediction of the storm would  
607 have led to a false alert, which means that the maneuver may have unnecessarily been car-  
608 ried out and might have led to a riskier, rather than safer, outcome. This approach is not  
609 specific to this storm but can be applied to storms in general, showing that a storm can  
610 possibly change the probability of collision, which can also result in making the wrong  
611 decision with regard to a collision avoidance maneuver, in one direction or the other.

612 **Figure 12.** Cumulative probability of collision as a function of time during the encounter. The scenario  
613 with the storm is in red and without the storm in blue. The vertical dashed lines represent the times of closest  
614 approach between the unperturbed orbits (indicated on the top left corner). The collision avoidance maneuver  
615 threshold ( $10^{-4}$ ) is represented with a black dashed line.

616 The minimum distance between the objects used to flag a collision also has an influ-  
617 ence on the effects of the storm on the probability of collision. This is investigated in Ta-  
618 ble 2. The effects of the geomagnetic storm increased with decreasing minimum distance  
619 of collision: the relative difference in the probability of collision increased with decreasing  
620 minimum distance (so did the absolute difference, not shown in Table 2).

621 The storm perturbed the orbits by increasing the distance at closest approach be-  
622 tween two objects in some cases, and by decreasing the distance at closest approach be-  
623 tween two objects in other cases, as explained in Section 4.1. The decrease in probability  
624 of collision shows that taking into account all possible conjunctions, the storm overall de-  
625 creased the total number of encounters in this particular example. In other words, there  
626 were more cases where it increased the distance at closest approach from a value below  
627 the minimum distance (without the storm) to a value above the minimum distance (with  
628 the storm) than cases where it decreased the distance at closest approach from a value  
629 above the minimum distance (without the storm) to a value below the minimum distance  
630 (with the storm).

631 The fact that the probability decreased more as a result of lowering the minimum  
632 distance of collision in the presence of a storm (Table 2) means that the number of con-  
633 junctions decreased more with the storm than without the storm if the minimum distance  
634 of collision was smaller. To understand why, consider a situation where the storm in-  
635 creased the distance at closest approach from 1.5 m (without the storm) to 4 m (with the  
636 storm). The situation is recorded as a collision with and without the storm if the mini-  
637 mum distance of collision was 5 m. If the minimum distance instead was 2 m, this situa-  
638 tion would still be recorded as a collision without the storm but it would not be recorded  
639 anymore as a collision with the storm. In other words, the total number of collisions with-  
640 out the storm would still be the same with the new threshold but it would be smaller by  
641 one conjunction in the presence of the storm.

Consequently, for lower probability of collisions ( $10^{-5}$ ,  $10^{-6}$  for instance), the relative difference is expected to be even greater. An application of this study is that there is often an unknown on the minimum distance of collision to set for the evaluation of the probability of collision. Recall that this distance corresponds to the sum of the two object radii only if the objects are spherical, which is not the case most of the time, particularly if the objects are satellites. Satellites can also have tethers or booms, such as the Challenging Mini-satellite Payload (CHAMP) satellite. Therefore, the attitude of the satellite has a direct influence on the minimum distance of collision. Unfortunately, a perfect knowledge of the attitude is almost always impossible, since the vast majority of objects in orbit have uncertain geometries and orientations, and resulting in uncertainties on the minimum distance of collision. This analysis shows that the effects of a miss prediction of a storm can possibly vary with the attitude of the spacecraft at the time of closest approach.

**Table 2.** Probability of collision with and without the geomagnetic storm for different values of the minimum distance of collision.

Min dist. collision (m)	$P_c$ with storm	$P_c$ without storm	Relative difference
5	0.001701	0.001559	9.1%
2	0.000338	0.000276	22.5%
1.2	0.000113	0.000088	28.4%
1.0	0.000073	0.000056	30.4%

## 5 Conclusion

The CARA algorithm developed in SpOCK uses a Monte Carlo approach to predict the probability of collision from the covariance matrices of the two objects at epoch. SpOCK propagates ensemble members, representing small perturbations on the initial positions and velocities, by modeling the perturbing forces such as the perturbations of the gravitational potential due to the asphericity and non-uniform mass distribution of the Earth, the atmospheric drag, the solar radiation pressure and the gravitational perturbations from the Moon and the Sun. More specifically, it uses a thermosphere model, either NRLMSISE or GITM, to accurately model the atmospheric density at the position of the spacecraft, hence the drag acceleration. While propagating the perturbed orbits, SpOCK screens for collisions between all ensemble members. Specifically, it interpolates the minimum distance between two objects with fifth order polynomials. If this distance is smaller



668 than the sum of the two object radii, it records the situation as a conjunction. After re-  
669 peating this operation for all ensemble members, SpOCK divides the total number of en-  
670 counters by the total number of cases, usually at least a hundred million, which approxi-  
671 mates the probability of collision.

672 Although atmospheric drag is one of the main perturbing forces for LEO orbits (rep-  
673 resenting 90% to 95% of the force in the in-track direction), uncertainties in the thermo-  
674 spheric density are usually not taken into account in collision risk assessment algorithms.  
675 Important uncertainties rely on the atmospheric density because the coupling of the upper  
676 atmosphere with the Earth space environment (the ionosphere and the magnetosphere) is  
677 not well understood, and because the solar activity, the main driver of this coupled system,  
678 is itself very hard to predict. CMEs, solar flares, and CIRs cause important and difficult  
679 to predict disturbances of the atmospheric density. Therefore, ignoring all these effects re-  
680 sults in important errors in the prediction of the probability of collision. The approach for  
681 taking into account the uncertainties in the solar activity to derive probability distribution  
682 functions of the probability of collision was introduced. Specifically, PDFs and CDFs of  
683 the probability of collision can be derived from distributions of historical forecast errors  
684 in the geomagnetic indices F10.7 and Ap. An example of such a PDF was provided for  
685 a simulated conjunction, and illustrated variations in the probability of collision of an or-  
686 der of magnitude. These PDFs and CDFs can assist operators in the determination of the  
687 true risk of collision in the presence of atmospheric density errors. An empirical method  
688 to determine the confidence interval associated with the predictions of the probability of  
689 collision was presented and showed that 95% of the runs resulted in values of the proba-  
690 bility collision less than 2.6% different from the median value. Although the Monte Carlo  
691 method was used in this study to predict the probability of collision, the overall approach  
692 is applicable to other methods, such as analytical methods.

693 Finally, the effects of geomagnetic storms on the probability of collision were illus-  
694 trated with an example of a parallel conjunction between two spacecraft two days after  
695 epoch. On March 17th, 2015, a strong storm hit the upper atmosphere, with values of  
696 the geomagnetic index Ap exceeding 200. Density enhancements by almost 50% at 400  
697 km strongly increased the drag, modifying the orbits of the satellites. The effects on the  
698 risk of collision led to differences up to 30% in the probability of collision, compared to  
699 a situation without a storm. This relative difference was shown to vary inversely with the  
700 minimum distance (i.e., the size of the objects). This analysis demonstrates the importance

701 of predicting geomagnetic storms. In this example, the miss prediction of the geomagnetic  
702 storm resulted in a false alert because the probability of collision without the storm was  
703 above the threshold for a collision avoidance maneuver.

#### 704 **Acknowledgments**

705 This research was funded by NASA grant NNL13AQ00C and was supported by AFOSR  
706 under DDDAS (Dynamic Data-Driven Applications Systems, <http://www.1dddas.org/>)  
707 grant FA9550-16-1-0071. We acknowledge use of NASA/GSFC's Space Physics Data  
708 Facility's OMNIWeb service and OMNI data, the Space Weather Prediction Center data  
709 from the National Oceanic and Atmospheric Administration, and the use of the Satellite  
710 Took Kit (STK) at Analytical Graphics, Inc. for the visualization of orbits. The data used  
711 are listed in the references, tables, and appendix.

712 **Appendix: Initial states and covariance matrices**

713 Distances are expressed in meters, and time in seconds.

$$\bar{U}_{1,40} = \begin{pmatrix} 202780.692 \\ -3873336.722 \\ -3336137.888 \\ 7644.314213 \\ 540.915272 \\ -493.855868 \end{pmatrix} \quad (7)$$

$$C_1 = \begin{pmatrix} 4.744089478916300000000000 & -1.2583279067770000000000 & 2.1279552605419000000000 & 0.00000000000000000000 & 0.00000000000000000000 & 0.00000000000000000000 \\ -1.2583279067770000000000 & 6.1279552605419000000000 & 2.1279552605419000000000 & 0.00000000000000000000 & 0.00000000000000000000 & 0.00000000000000000000 \\ 0.0000000000000000000000 & 0.00000000000000000000 & 0.00000000000000000000 & 0.00000000000000000000 & 0.00000000000000000000 & 0.00000000000000000000 \\ 0.0000000000000000000000 & 0.00000000000000000000 & 0.00000000000000000000 & 0.0000010000000000000000 & 0.0000010000000000000000 & -0.0000010000000000000000 \\ 0.0000000000000000000000 & 0.00000000000000000000 & 0.00000000000000000000 & 0.00000000000000000000 & 0.00000000000000000000 & 0.0000010000000000000000 \end{pmatrix} \quad (8)$$

$$\bar{U}_{2,40} = \begin{pmatrix} 558232.011 \\ -3649646.379 \\ -5675244.936 \\ 6569.617992 \\ 3593.547352 \\ -1664.494700 \end{pmatrix} \quad (9)$$

$$C_2 = \begin{pmatrix} 4.7439512624715000000000 & -1.25825500004600000000 & 2.12802436727500000000 & 0.000000000000000000 & 0.000000000000000000 & 0.000000000000000000 \\ -1.25825500004600000000 & 6.12802436727500000000 & 2.12802436727500000000 & 0.000000000000000000 & 0.000000000000000000 & 0.000000000000000000 \\ 0.00000000000000000000 & 0.000000000000000000 & 0.000000000000000000 & 0.000000000000000000 & 0.000000000000000000 & 0.000000000000000000 \\ 0.00000000000000000000 & 0.000000000000000000 & 0.000000000000000000 & 0.00000100000000000000 & 0.00000100000000000000 & -0.00000100000000000000 \\ 0.00000000000000000000 & 0.000000000000000000 & 0.000000000000000000 & 0.000000000000000000 & 0.000000000000000000 & 0.00000100000000000000 \end{pmatrix} \quad (10)$$

716  
717  
718  
719  
720  
721  
722  
723  
724  
725  
726  
727  
728  
729  
730  
731  
732  
733  
734  
735  
736  
737  
738  
739  
740  
741  
742  
743  
744  
745  
746  
747

## References

## References

- Aida, S., M. Kirschner, and F. Meissner (2015), Collision risk assessment and mitigation strategy for the gsoc geo satellites.
- Akella, M. R., and K. T. Alfriend (2000), Probability of collision between space objects, *Journal of Guidance, Control, and Dynamics*, 23(5), 769–772.
- Alfano, S. (1994), Determining satellite close approaches, *Journal of the Astronautical Sciences*, 42, 143–152.
- Alfano, S. (2005a), A numerical implementation of spherical object collision probability, *Journal of the Astronautical Sciences*, 53(1), 103.
- Alfano, S. (2005b), Beta conjunction analysis tool, *AAS/AIAA Astrodynamics Specialist Conference*.
- Alfano, S. (2006), Addressing nonlinear relative motion for spacecraft collision probability, in *AAS/AIAA Astrodynamics Specialist Conference, Keystone, CO., Paper*, vol. 6760.
- Alfano, S. (2009), Satellite conjunction monte carlo analysis, *AAS Spaceflight Mechanics Mtg, Savannah, GA, Paper*, pp. 09–233.
- Alfriend, K. T., M. R. Akella, J. Frisbee, J. L. Foster, D.-J. Lee, and M. Wilkins (1999), Probability of collision error analysis, *Space Debris*, 1(1), 21–35.
- Bruinsma, S., J. M. Forbes, R. S. Nerem, and X. Zhang (2006), Thermosphere density response to the 20-21 November 2003 solar and geomagnetic storm from CHAMP and GRACE accelerometer data, *Journal of Geophysical Research (Space Physics)*, 111, A06303, doi:10.1029/2005JA011284.
- Bruinsma, S. L., and J. M. Forbes (2007), Global observation of traveling atmospheric disturbances (tads) in the thermosphere, *Geophysical Research Letters*, 34(14).
- Bussy-Virat, C., J. Getchius, and A. Ridley (2018), The spacecraft orbital characterization kit and its applications to the cygnss mission., in *2018 Space Flight Mechanics Meeting*, p. 1973.
- Chan, F. (2008), *Spacecraft collision probability*, Aerospace Press.
- D. Pachura, M. D. H. (2016), Conjunction Assessment Late-Notice High-Interest Event Investigation: Space Weather Aspects, *NASA robotic CARA*.
- Dagum, P., R. Karp, M. Luby, and S. Ross (2000), An optimal algorithm for monte carlo estimation, *SIAM Journal on computing*, 29(5), 1484–1496.

- 748 Emmert, J. (2015), Thermospheric mass density: A review, *Advances in Space Research*,  
749 56(5), 773–824.
- 750 Emmert, J., J. Byers, H. Warren, and A. Segerman (2014), Propagation of forecast errors  
751 from the sun to leo trajectories: How does drag uncertainty affect conjunction frequency?,  
752 *Tech. rep.*, DTIC Document.
- 753 Emmert, J., H. Warren, A. Segerman, J. Byers, and J. Picone (2016), Propagation of atmo-  
754 spheric density errors to satellite orbits, *Advances in Space Research*.
- 755 Foster, J. (2001), The analytical basis for debris avoidance operations for the international  
756 space station and space shuttle, *Orbital Debris Quarterly News*, 6(2), 11.
- 757 Hejduk, M., and R. Frigm (2015), Collision Avoidance Short Course - Part I: Theory, *NASA*  
758 *robotic CARA*.
- 759 Horsley, M. (2012), Satellite re-entry modeling and uncertainty quantification, in *Advanced*  
760 *Maui Optical and Space Surveillance Technologies Conference*, vol. 1, p. 52.
- 761 Lei, J., J. P. Thayer, W. Wang, and R. L. McPherron (2011), Impact of cir storms on ther-  
762 mosphere density variability during the solar minimum of 2008, *Solar Physics*, 274(1-2),  
763 427–437.
- 764 Liou, J.-C. (2016), The Orbital Debris Problem, *Space Tech Conference*.
- 765 Moe, K., and M. M. Moe (2005), Gas surface interactions and satellite drag coefficients,  
766 *Planetary Space Science*, 53, 793–801, doi:10.1016/j.pss.2005.03.005.
- 767 Newman, L. K. (2016), NASA Conjunction Assessment Risk Analysis Approach, *NASA*  
768 *robotic CARA*.
- 769 Patera, R. P. (2001), General method for calculating satellite collision probability, *Journal of*  
770 *Guidance, Control, and Dynamics*, 24(4), 716–722.
- 771 Patera, R. P. (2005), Calculating collision probability for arbitrary space vehicle shapes via  
772 numerical quadrature, *Journal of guidance, control, and dynamics*, 28(6), 1326–1328.
- 773 Pawlowski, D. J., and A. J. Ridley (2011), The effects of different solar flare characteristics  
774 on the global thermosphere, *Journal of Atmospheric and Solar-Terrestrial Physics*, 73(13),  
775 1840–1848.
- 776 Picone, J., A. Hedin, D. P. Drob, and A. Aikin (2002), Nrlmsise-00 empirical model of the  
777 atmosphere: Statistical comparisons and scientific issues, *Journal of Geophysical Re-*  
778 *search: Space Physics*, 107(A12).
- 779 Ridley, A., Y. Deng, and G. Toth (2006), The global ionosphere–thermosphere model, *Jour-*  
780 *nal of Atmospheric and Solar-Terrestrial Physics*, 68(8), 839–864.

- 781 Sanchez-Ortiz, N., R. Domínguez-González, H. Krag, and T. Flohrer (2015), Impact on  
782 mission design due to collision avoidance operations based on tle or csm information, *Acta*  
783 *Astronautica*, 116(Complete), 368–381, doi:10.1016/j.actaastro.2015.04.017.
- 784 Schilling, B., Y. Taleb, J. R. Carpenter, M. Balducci, and T. W. Williams (2016), Operational  
785 experience with the wald sequential probability ratio test for conjunction assessment from  
786 the magnetospheric multiscale mission, in *AIAA/AAS Astrodynamics Specialist Confer-*  
787 *ence*, p. 5424.
- 788 Stoll, E., B. D’Souza, B. B. Virgili, K. Merz, and H. Krag (2013), Operational collision  
789 avoidance of small satellite missions, in *Aerospace Conference, 2013 IEEE*, pp. 1–11, doi:  
790 10.1109/AERO.2013.6496955.
- 791 Storz, M. F., B. R. Bowman, M. J. I. Branson, S. J. Casali, and W. K. Tobiska (2005), High  
792 accuracy satellite drag model (hasdm), *Advances in Space Research*, 36(12), 2497–2505.
- 793 Sutton, E. K., J. M. Forbes, and R. S. Nerem (2005), Global thermospheric neutral den-  
794 sity and wind response to the severe 2003 geomagnetic storms from CHAMP ac-  
795 celerometer data, *Journal of Geophysical Research (Space Physics)*, 110, A09S40, doi:  
796 10.1029/2004JA010985.
- 797 Sutton, E. K., J. M. Forbes, R. S. Nerem, and T. N. Woods (2006), Neutral density response  
798 to the solar flares of October and November, 2003, *Geophysical Research Letters*, 33,  
799 L22101, doi:10.1029/2006GL027737.
- 800 Vallado, D., and W. McClain (2007), *Fundamentals of Astrodynamics and Applications*,  
801 *Third Edition*, Space Technology Library, Microcosm Press and Springer.
- 802 Vallado, D. A., and D. Finkleman (2014), A critical assessment of satellite drag  
803 and atmospheric density modeling, *Acta Astronautica*, 95, 141–165, doi:  
804 10.1016/j.actaastro.2013.10.005.

Figure 1.

Author Manuscript



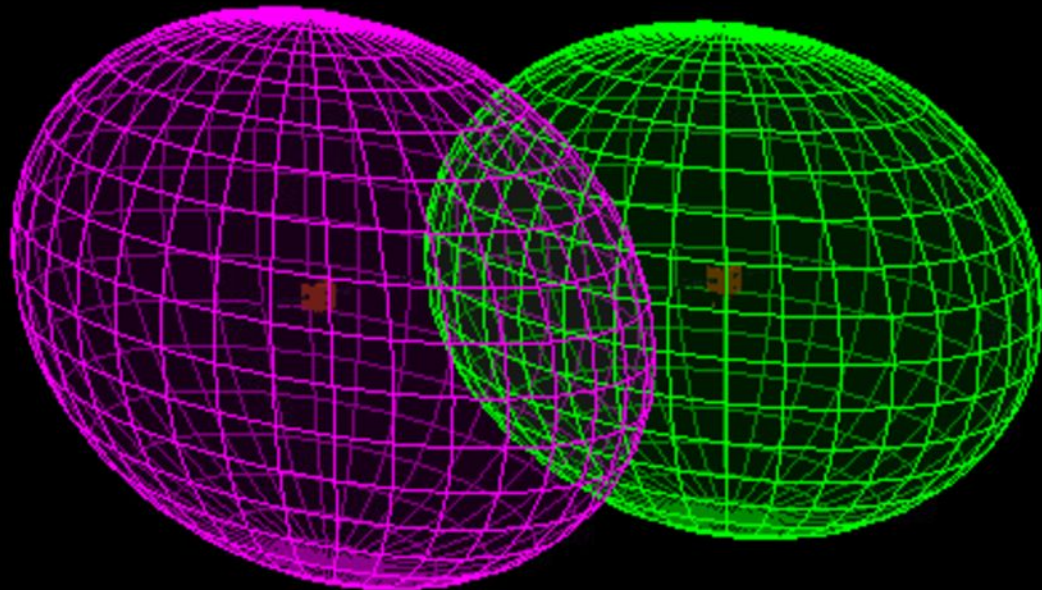
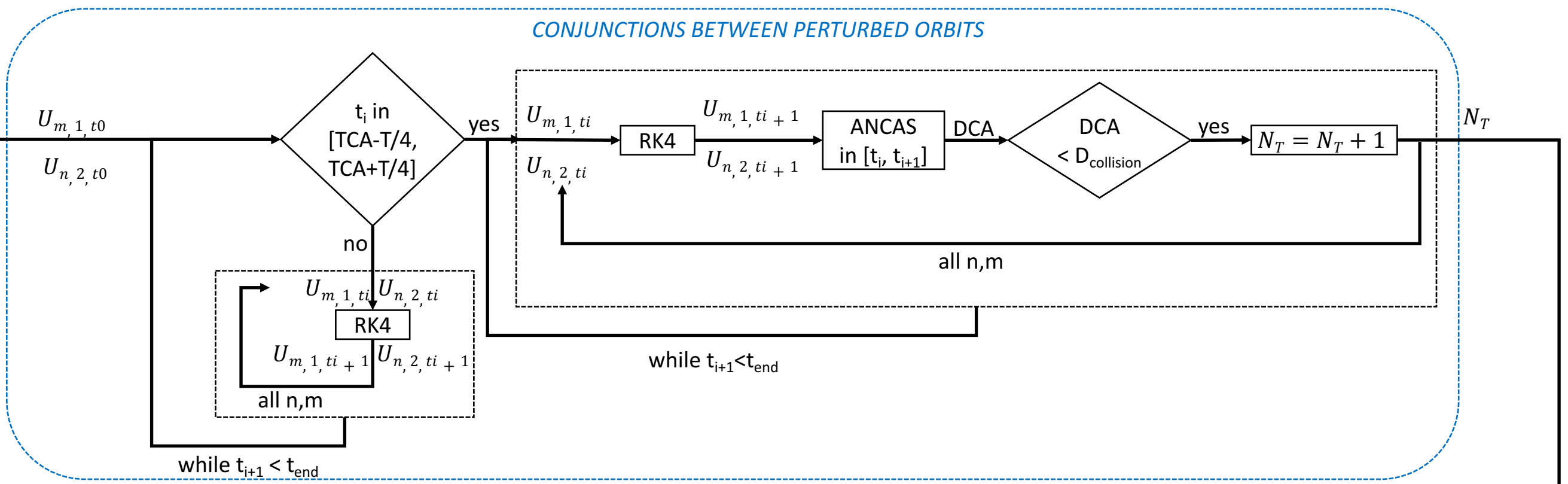
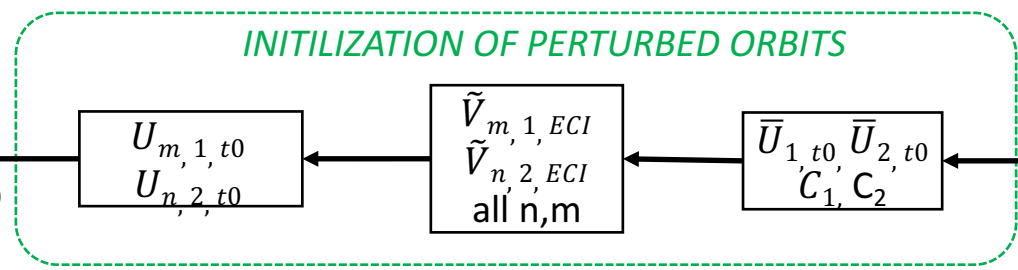
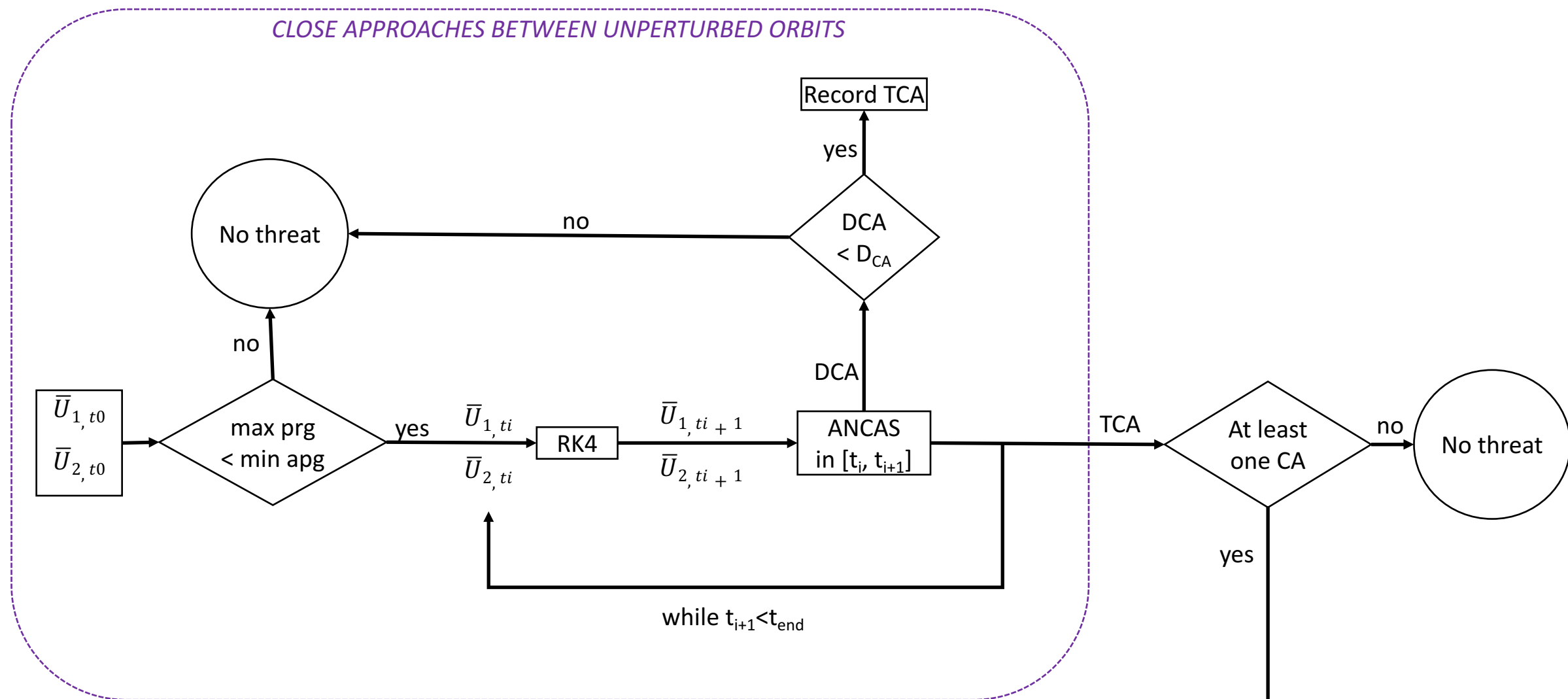


Figure 2.

Author Manuscript



$$P_c = \frac{N_T}{N_E^2}$$

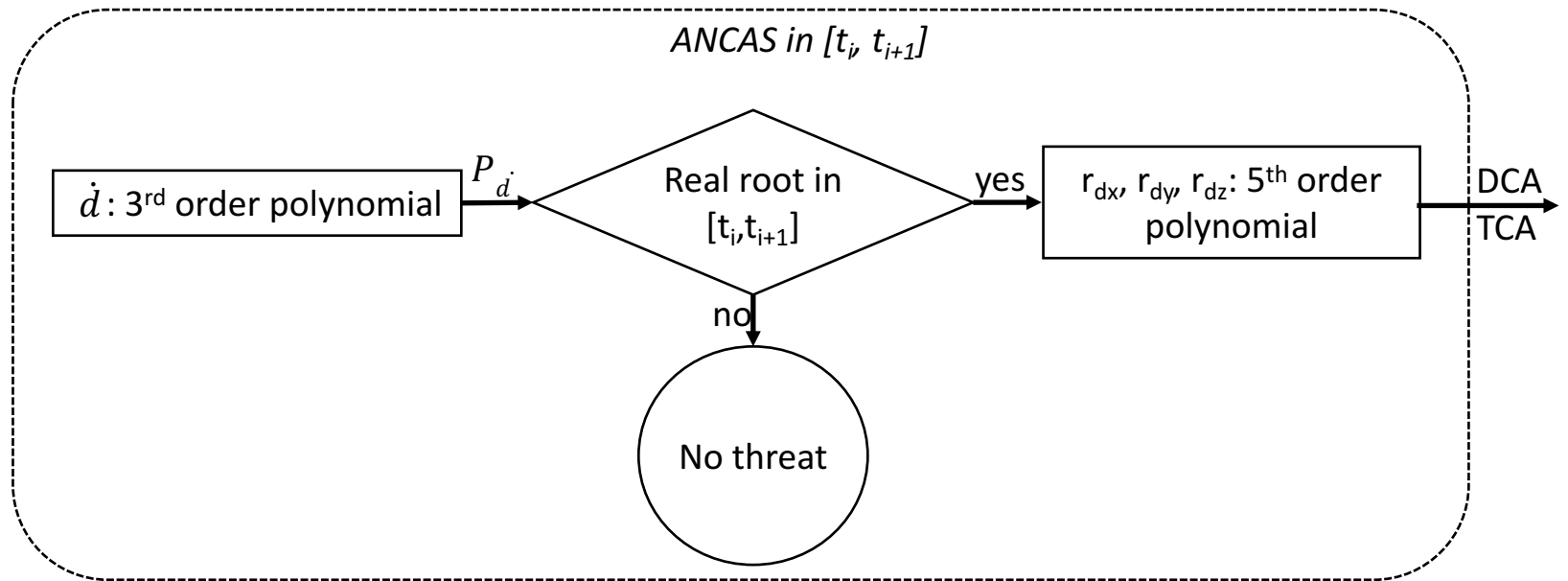


Figure 3.

Author Manuscript

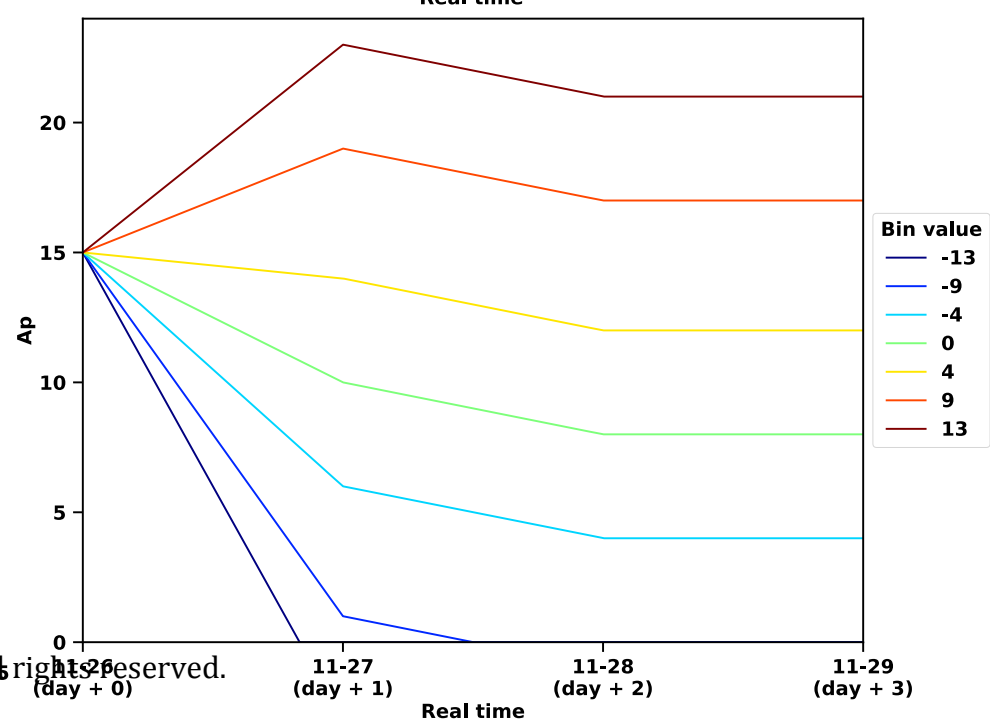
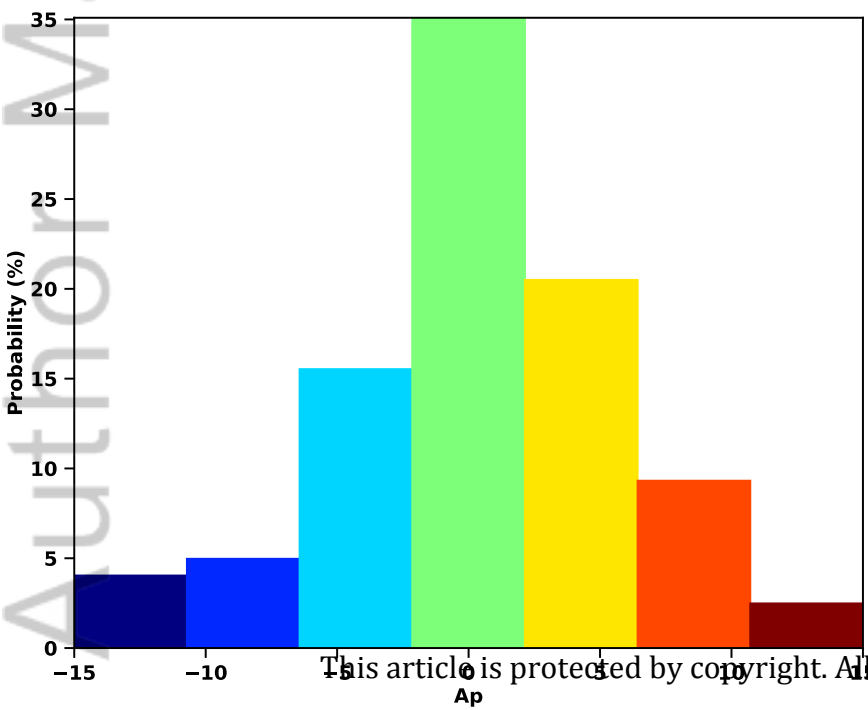
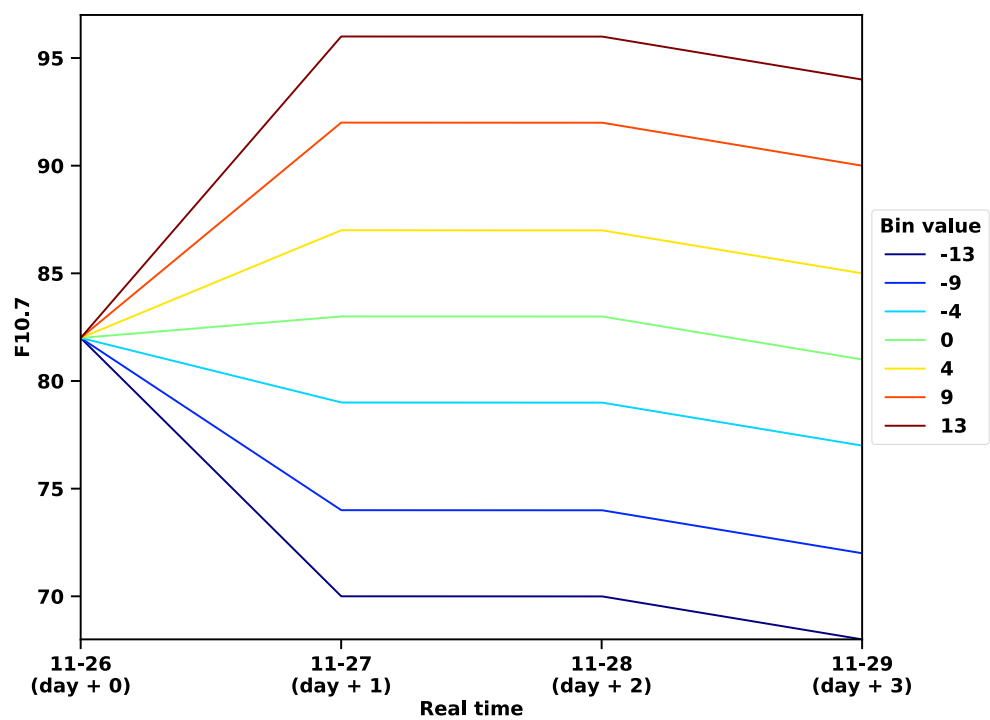
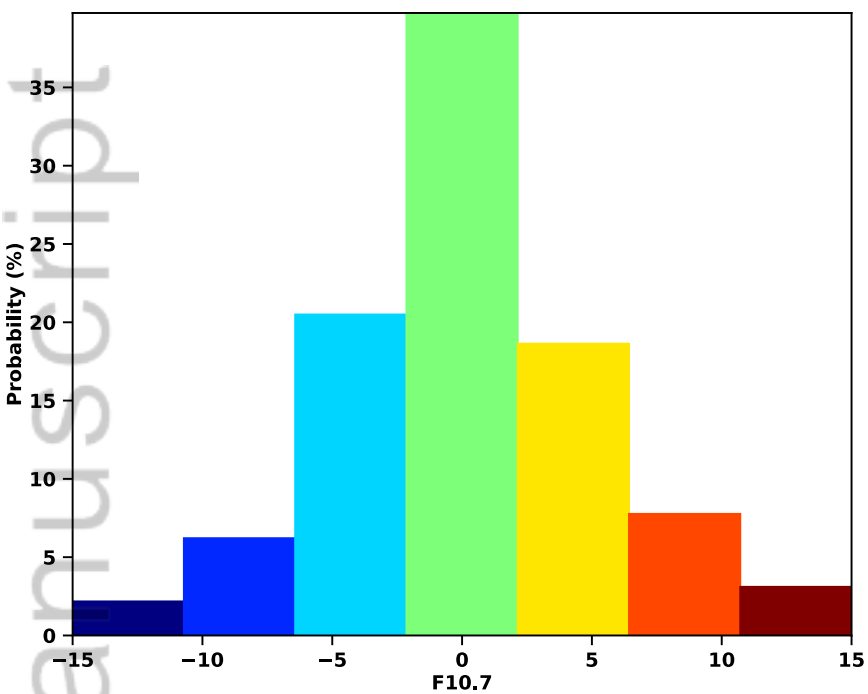


Figure 4.

Author Manuscript

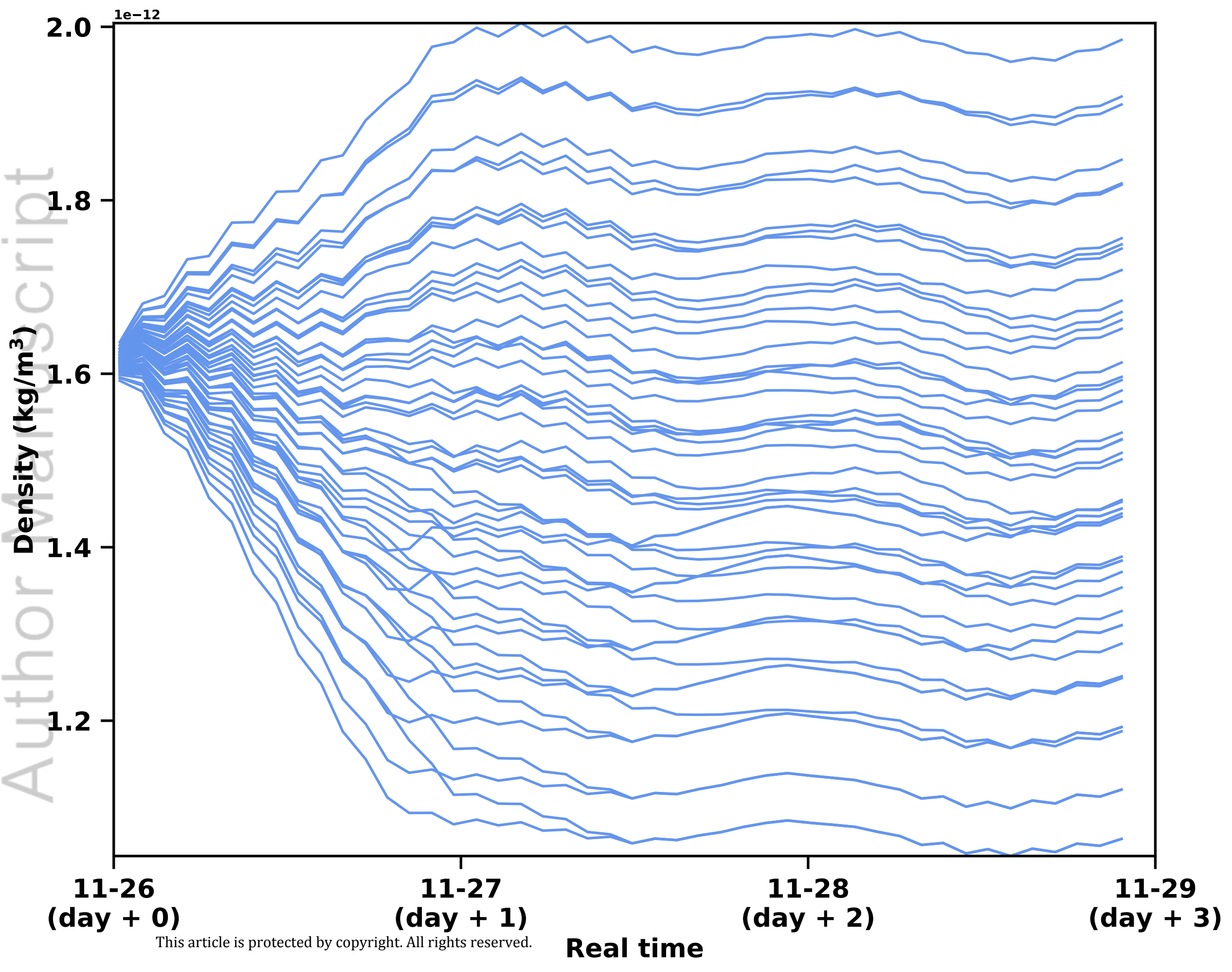


Figure 5.

Author Manuscript



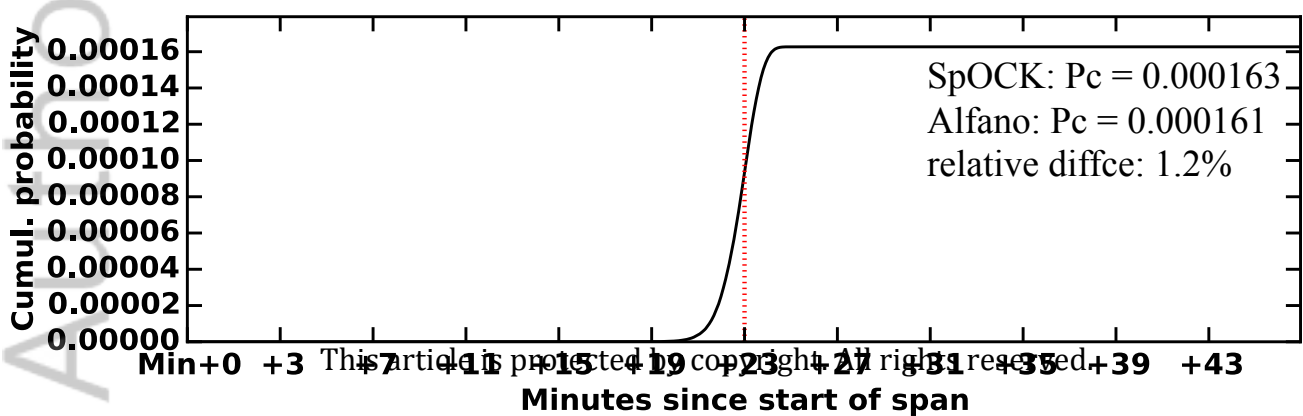
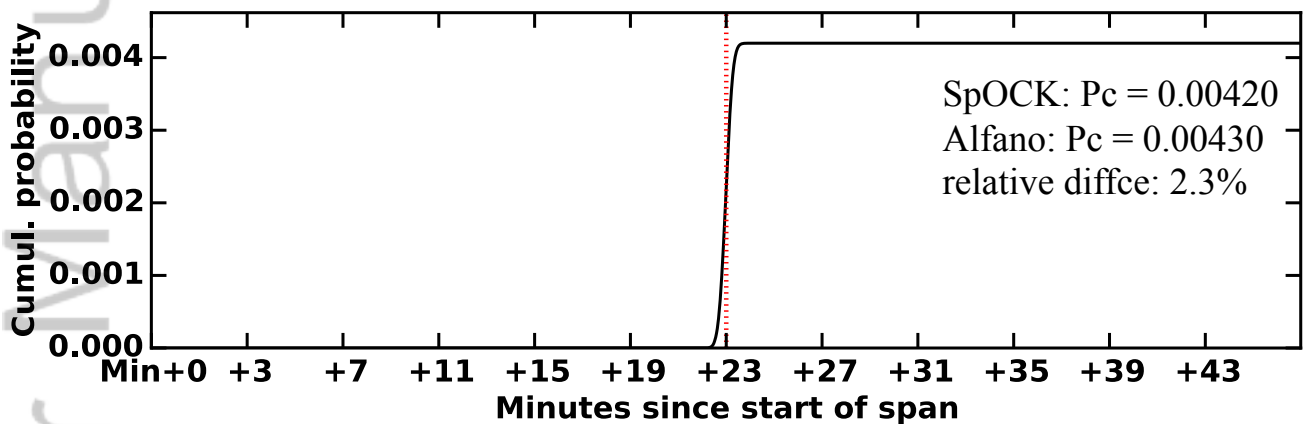
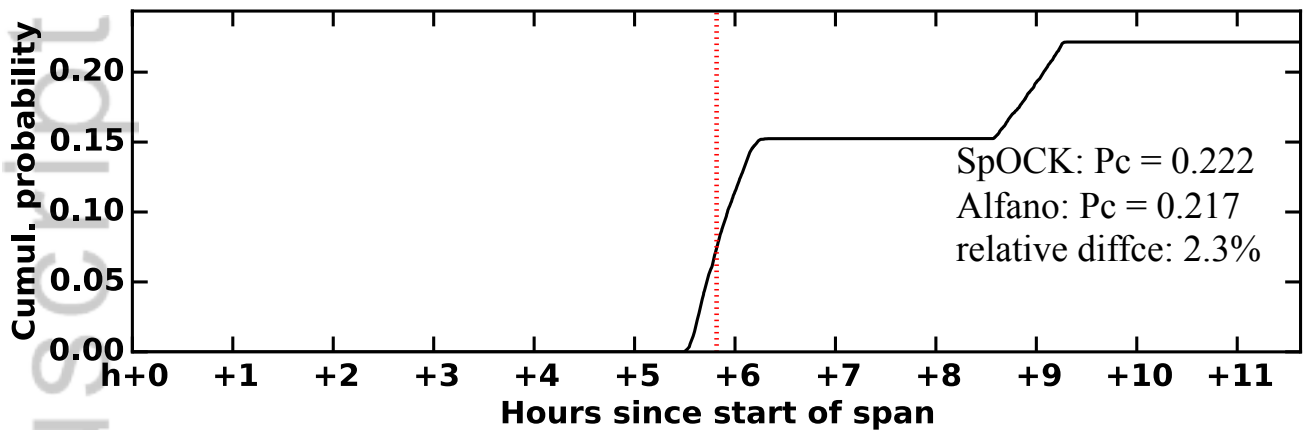


Figure 6.

Author Manuscript

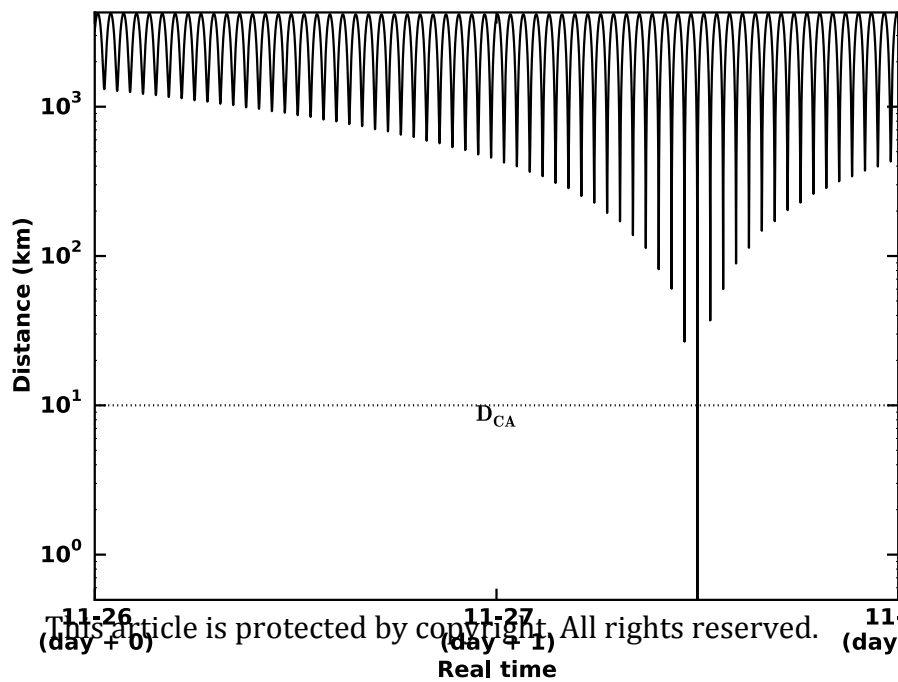
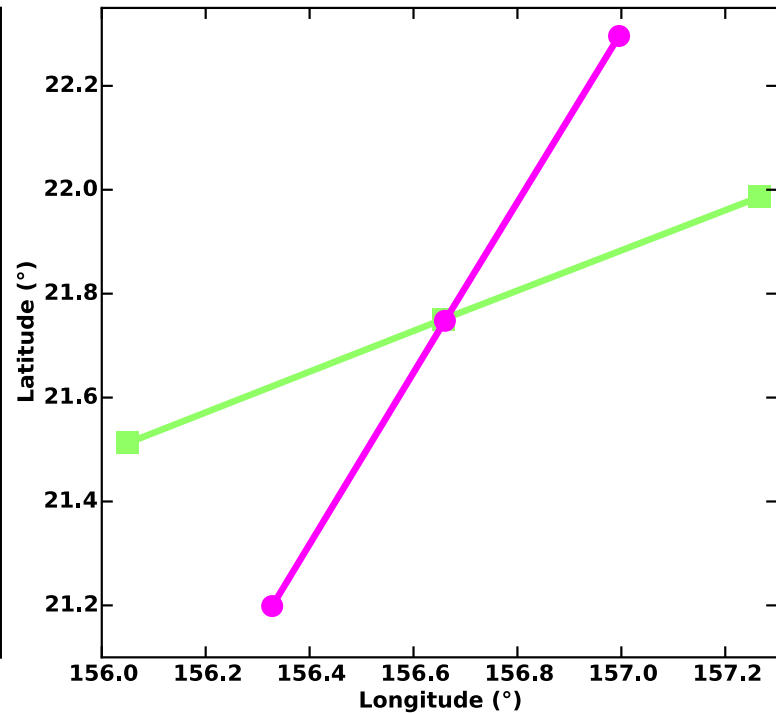
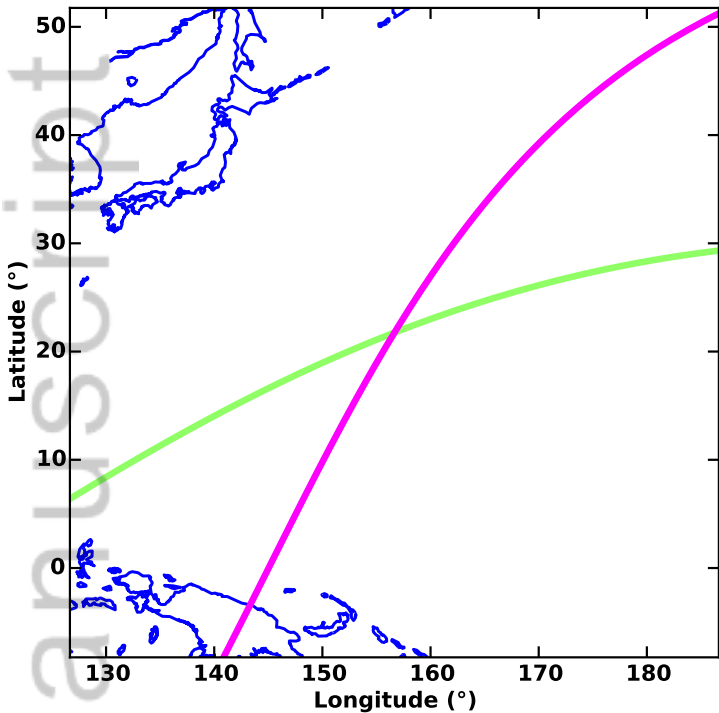


Figure 7.

Author Manuscript

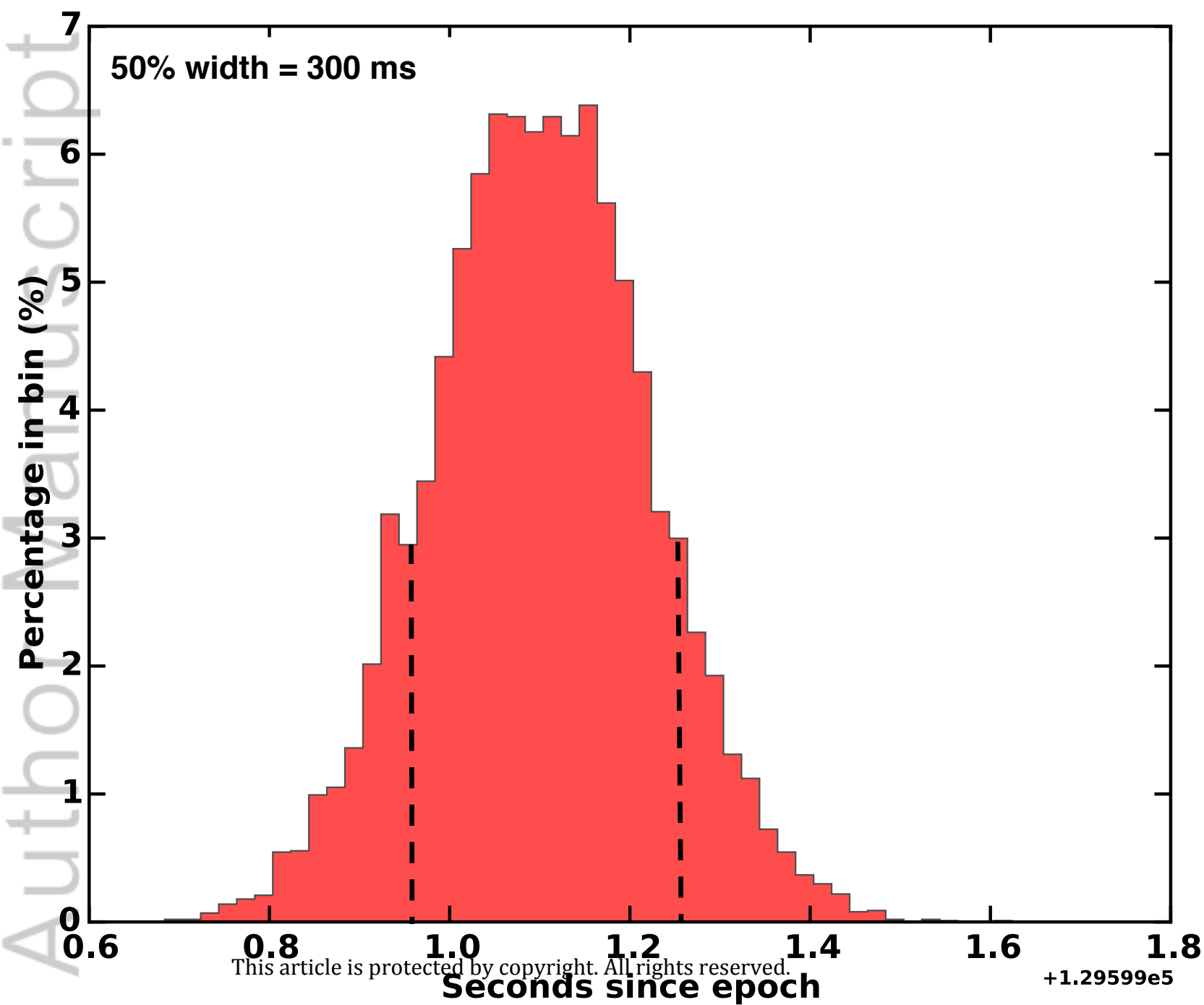
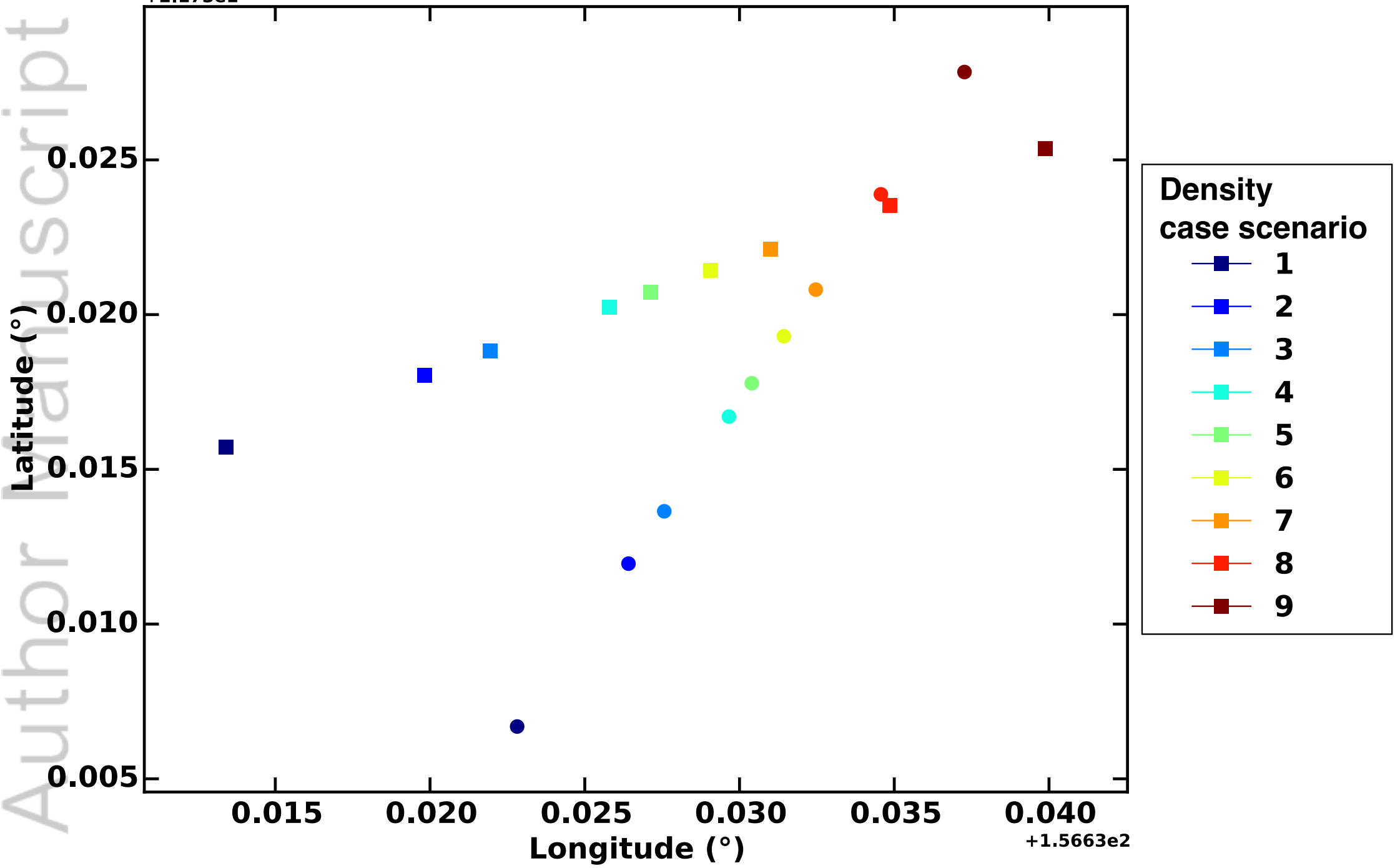


Figure 8.

Author Manuscript

+2.173e1

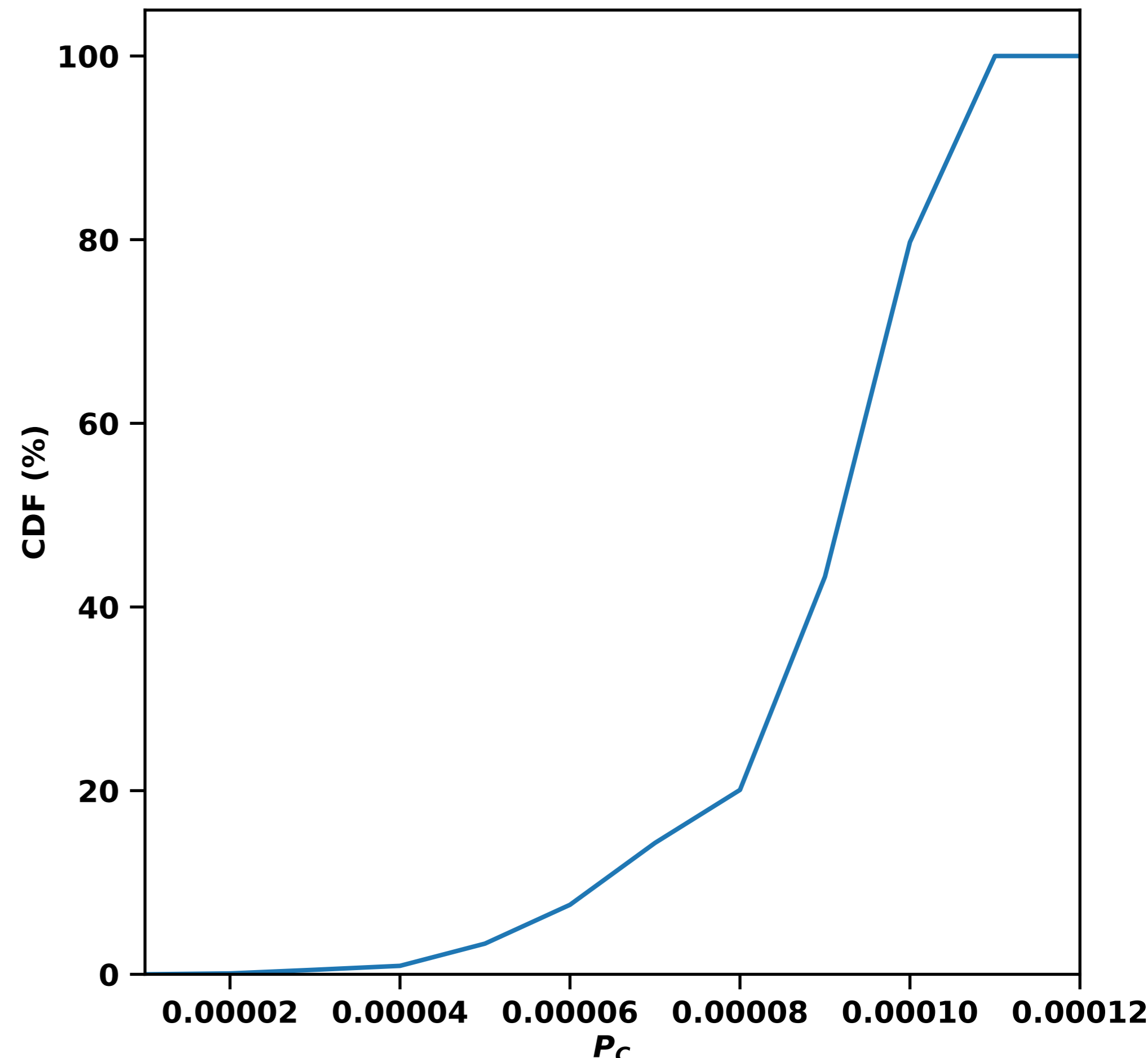
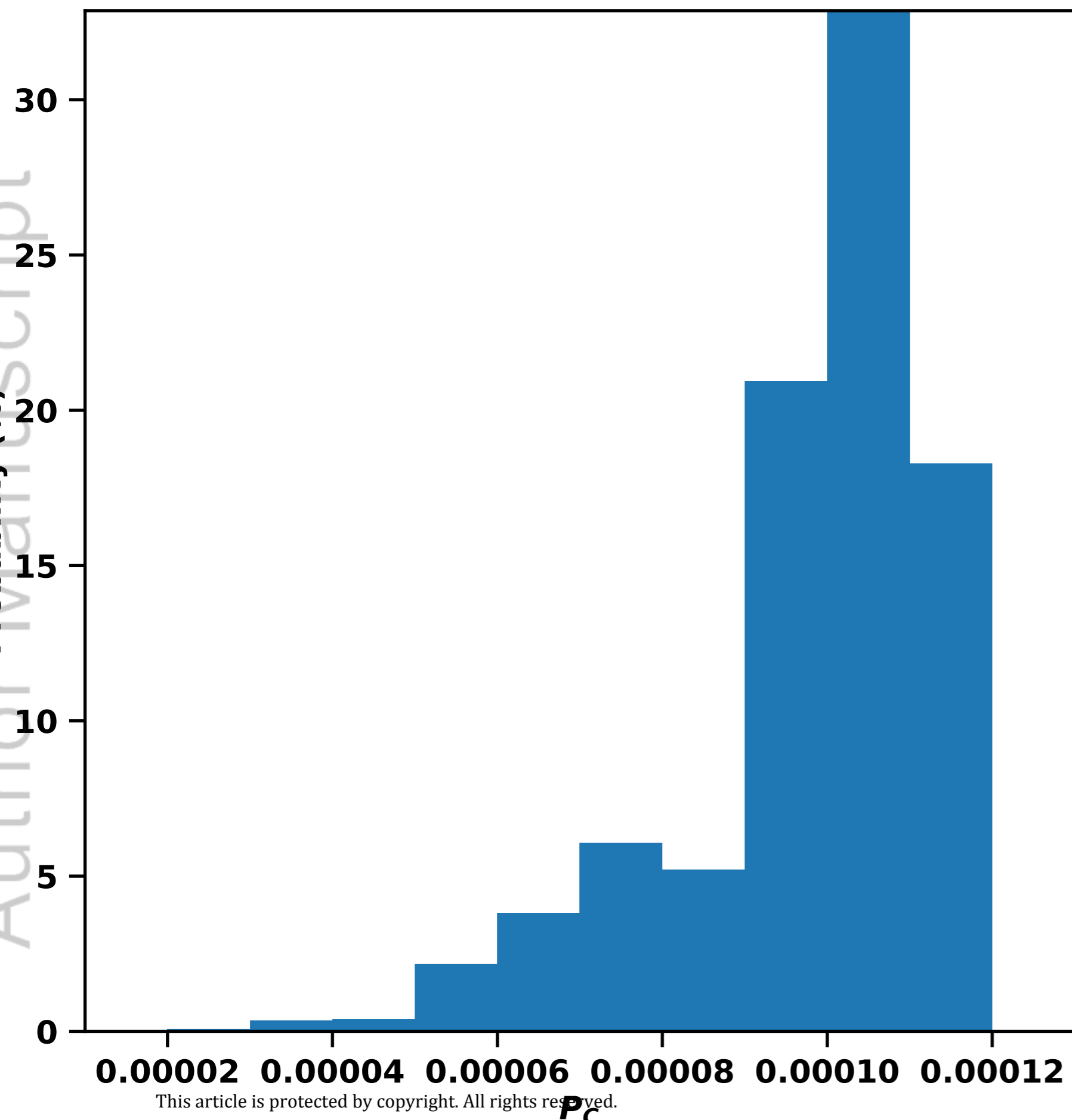


+1.5663e2

Figure 9.

Author Manuscript







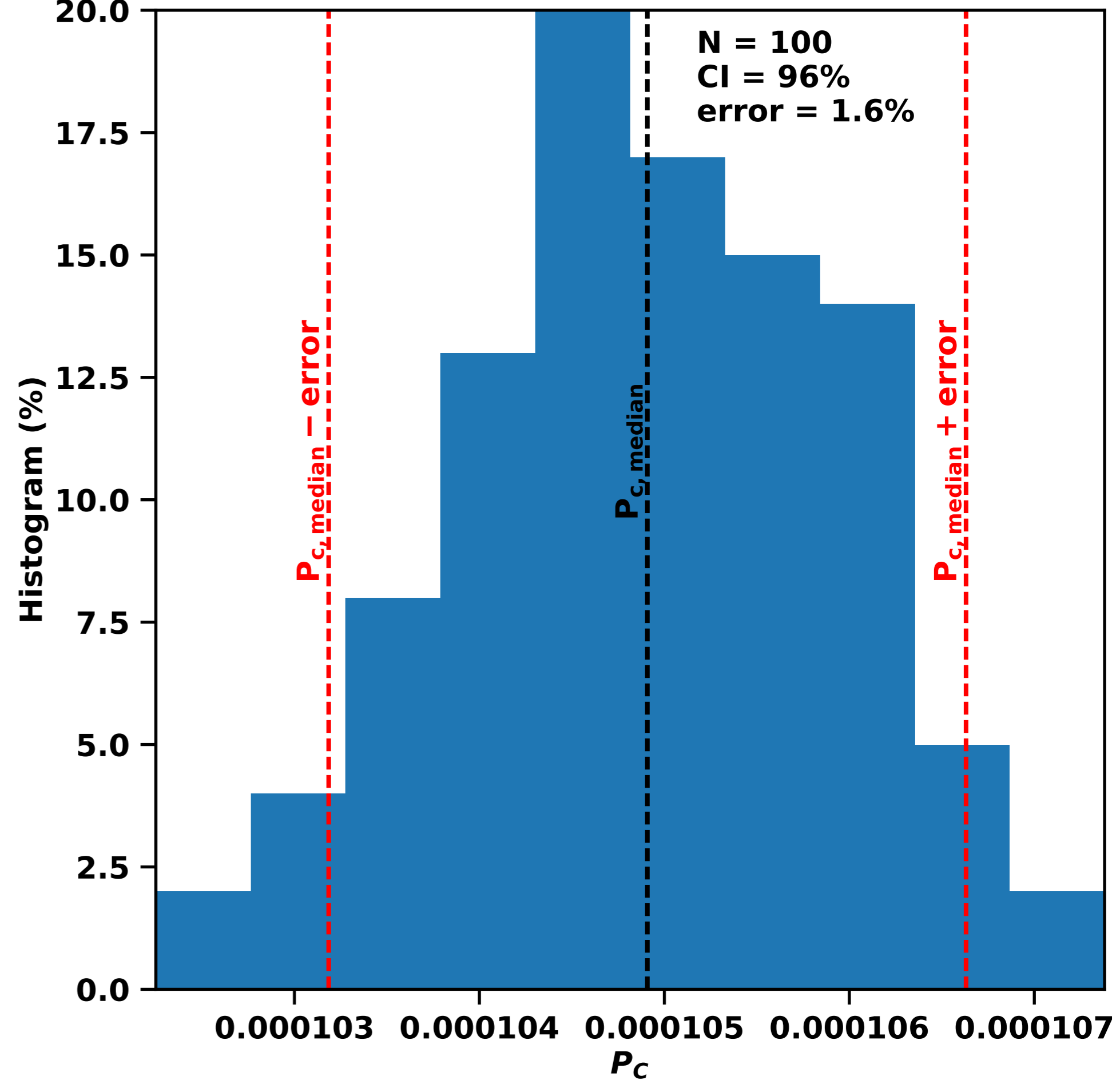
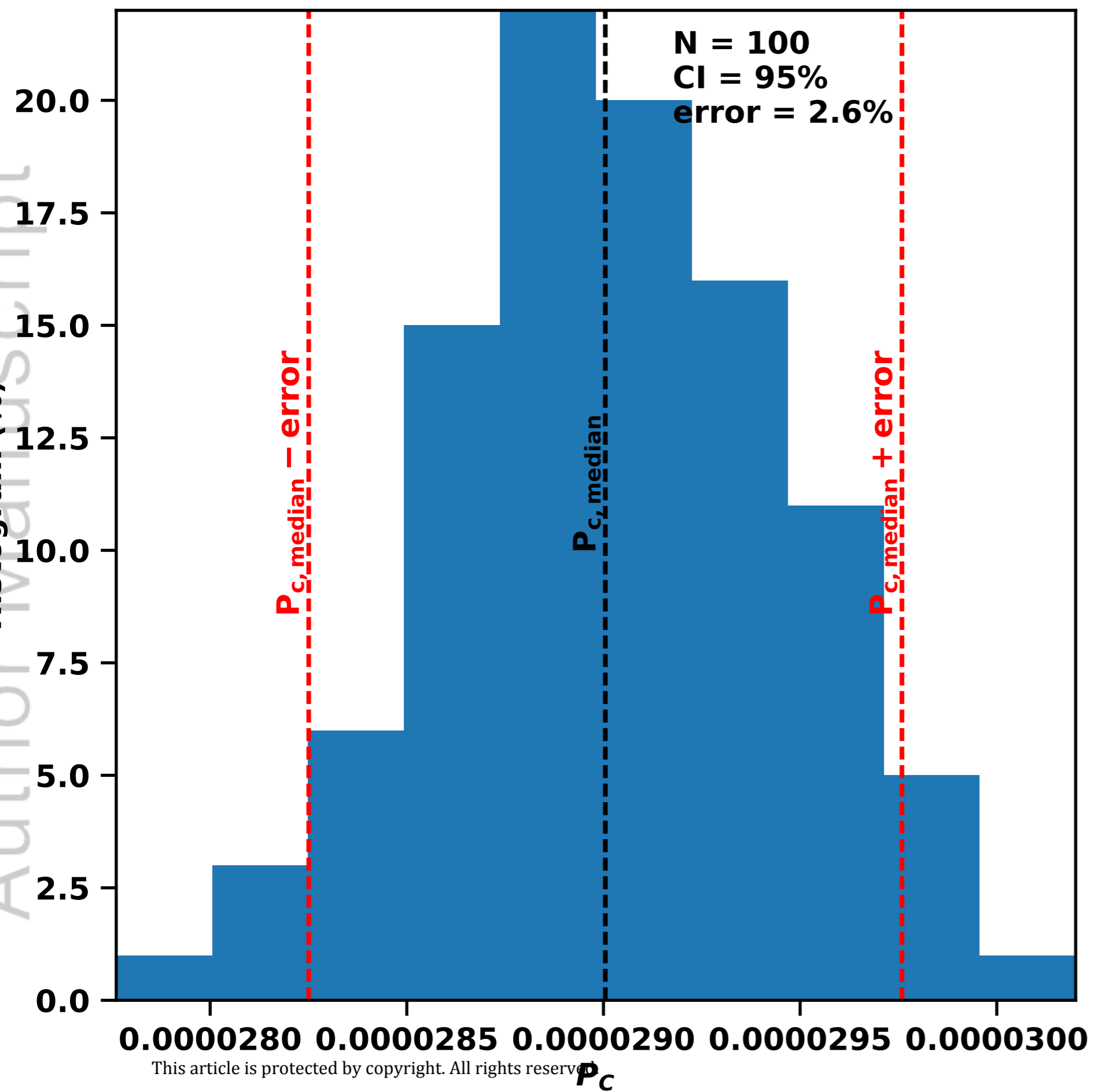


Figure 11.

Author Manuscript

Author Manuscript

